

This item was submitted to [Loughborough's Research Repository](#) by the author.
Items in Figshare are protected by copyright, with all rights reserved, unless otherwise indicated.

Simulations of stably stratified flow past two spheres at $Re = 300$

PLEASE CITE THE PUBLISHED VERSION

<https://doi.org/10.1063/5.0044801>

PUBLISHER

AIP Publishing

VERSION

AM (Accepted Manuscript)

PUBLISHER STATEMENT

This article may be downloaded for personal use only. Any other use requires prior permission of the author and AIP Publishing. This article appeared in Cocetta, F., Szmelter, J. and Gillard, M. (2021). Simulations of stably stratified flow past two spheres at $Re = 300$. *Physics of Fluids*, 33(4): 046602 and may be found at <https://doi.org/10.1063/5.0044801>

LICENCE

In Copyright

REPOSITORY RECORD

Cocetta, F, Joanna Szmelter, and Mike Gillard. 2021. "Simulations of Stably Stratified Flow Past Two Spheres at $Re = 300$ ". Loughborough University. <https://hdl.handle.net/2134/14387609.v1>.

Simulations of stably-stratified flow past two spheres at $Re=300$

F. Cocetta, J. Szmelter,^{a)} and M. Gillard
Loughborough University, Leicestershire LE11 3TU, UK

(Dated: 6 March 2021)

Flows past two spheres immersed in a horizontally moving, linearly-stratified fluid are investigated at a moderate Reynolds number of 300. Characterisation of flow patterns considers representative geometrical configurations defined by varying both the distance between the spheres and their relative orientation to the free stream direction. Simulations are performed on unstructured meshes chosen to accurately resolve the dynamics of fluids in regions close to the spheres for Froude numbers $Fr \in [0.25, \infty]$. Results illustrate the evolution of boundary layers, separation, and the wakes interaction under the influence of a gravity induced buoyancy force. Computations utilise a limited area, nonhydrostatic model employing Non-oscillatory Forward-in-Time (NFT) integration based on the Multidimensional Positive Definite Advection Transport Algorithm (MPDATA). The model solves the Navier-Stokes equations in the incompressible Boussinesq limit, suitable for describing a range of mesoscale atmospheric flows. Results demonstrate that stratification progressively dominates the flow patterns as the Froude number decreases and that the interactions between the two spheres' wakes bear a resemblance to atmospheric flows past hills.

I. INTRODUCTION

Intricate perturbations induced by a configuration of two spheres immersed in a stratified flow are representative of patterns typical of stratified flows past multiple generic obstacles. The study of such systems is relevant to geophysical flows, such as airflows over complex terrain and the associated mesoscale phenomena. Examples include flows past mountain ranges and the weather conditions within a valley, resulting from the interaction between the large-scale flow and flow driven by local conditions¹. Features such as lee waves, dividing streamline height, low-pressure zones behind obstacles, and the drag coefficient are affected by the valley's width, driving both constructive and destructive interferences². A sphere is traditionally used as a canonical shape in experimental investigations to gain insights into the physical processes common to atmospheric flows past orography. Flow structures past a single sphere have strong commonalities with flows past isolated hills, as can be observed for example by comparing simulations in Ref. 3 or Ref. 4 with those reported in Refs. 5–7. This interest can be extended to experiments involving configurations of multiple obstacles relevant, for example, to the design of wind turbine farms or to oceanographic applications, where spheres can represent archipelagos in different configurations, flows past complex bathymetry⁸, and marine appliances submersed in thermoclines⁹.

Flow structures developing in stratified flows past a single sphere have been explored both experimentally^{10,11} and computationally; e.g. Refs. 12 and 13. Numerical studies of a particular interest here, which explicitly represent a sphere in a computational domain using body fitted meshes, include Refs. 3, 4, and 14 and references therein. Flow patterns past an isolated sphere have been observed and classified for wide ranges of Froude, $Fr = V_o/Nh$, and Reynolds, $Re = V_oL/\nu$, numbers; V_o , N , h , L , and ν represent free stream velocity, buoyancy frequency, obstacle height, characteristic length

scale, and kinematic viscosity, respectively. Stratified flows produce a gravity-induced restorative buoyancy force, as fluid parcels are displaced from their hydrostatically balanced equilibrium position⁴. At moderate Reynolds numbers the three main distinct flow patterns, identified in Ref. 10, are: a non-axisymmetric attached vortex, lee-wave instability regime, and two-dimensional vortex shedding. These regimes are briefly reviewed below, in preparation for the discussion of results presented in sections III and IV.

At Reynolds number $Re = 300$, a neutrally-stratified flow past a sphere generates periodic shedding consisting of hairpin vortices¹⁵ with time-independent planar symmetry defined by the initially induced vortex. For very low stratification (i.e. $Fr \geq 10$) the characteristic structures of the neutrally-stratified flow are retained, however the plane of symmetry moves to the horizontal plane coinciding with the sphere's centre. As stratification increases, buoyancy forcing flattens the wake and inhibits vortex shedding – bringing the flow to a steady-state. The resulting pattern is characterised by a double wake structure, deformed in the vertical doughnut-shaped vortex ring in the lee of the sphere, and gravity wave radiation¹⁰. This flow regime is called non-axisymmetric attached vortex¹.

The peak of gravity wave amplitude occurs at $Fr \approx 1$, corresponding with the establishment of the lee-wave instability pattern. At this level of stratification, fluid parcels below the dividing streamline height (cf. Ref. 15) are forced to pass around the sides of the obstacle rather than over it, developing into a horizontal bi-dimensional recirculation behind the sphere. Fluid parcels above the dividing streamline height contribute to the production of gravity waves in the lee of the sphere. Together, the two flow structures constitute the lee-wave instability regime.

For approximately $Fr < 0.56$, the flow pattern changes into two-dimensional vortex shedding set in the horizontal plane. The characteristic feature of this regime are fluid parcels travelling around the sphere, producing a periodic motion similar to that observed for a flow past a cylinder. In numerical sim-

^{a)}Electronic mail: Author to whom correspondence should be addressed. E-mail address: j.szmelter@lboro.ac.uk

¹ Hereafter, we adopt the nomenclature of flow patterns reported in Ref. 10.

ulations, the two-dimensional vortex shedding regime is slow to develop, therefore a sufficiently long computational time is required for the regime to become correctly established, cf. Refs. 3 and 16.

The present work builds on our earlier studies of linearly-stratified flows past a sphere at $Re = 200$ and $Re = 300$ ^{3,15} and extends them to flows past two spheres for a range of Froude numbers $Fr \in [0.25, \infty]$. A moderate Reynolds number ($Re = 300$) is selected in order to avoid uncertainty related to turbulence modelling and to facilitate comparisons with cases of neutrally-stratified flows. Furthermore, historically the experimental data for stratified flows past a sphere also concentrated on low Reynolds numbers due to ease of measurement. However, our study in Ref. 3 and the study in Ref. 4 show that as stratification increases, the key flow patterns depend on viscosity only slightly. It is therefore likely that the presented results are also relevant to flows with higher Reynolds numbers. The study reported here considers configurations of two identical spheres; obtained by varying the distance between the spheres and their orientation relative to the free stream direction.

Studies of neutrally-stratified flows for a variety of geometrical arrangements of two spheres have been documented in e.g. Refs. 17–22, with Ref. 23 extending the study to a flow past in-line spheres. However, to the best of our knowledge this is the first comprehensive investigation of stratified flows past two spheres. We present a systematic characterisation of flow patterns, complemented by a quantitative analysis of drag coefficients, separation angles, and vortex-shedding frequencies. Simulations suggest vortex characteristics vary significantly with the relative placement of the spheres when in close proximity to each other. This is particularly pronounced for weakly-stratified flows, whereas at lower Froude numbers the flow patterns are dominated by stratification. As stratification increases, buoyancy effects progressively overcome viscosity, however the effects of vortex interactions and upstream objects blocking the incoming flow remain present.

Computations adopt an MPI-parallelised, Non-oscillatory Forward-in-Time Finite Volume (NFT-FV) approach^{3,15}. The numerical scheme integrates the Navier-Stokes equations under gravity in the incompressible Boussinesq limit. Finite volume discretisation is implemented on flexible unstructured/prismatic meshes that are particularly well suited to represent various configurations of two spheres and to capture details of flow patterns. The validity of the NFT-FV scheme operating on unstructured meshes has been successfully demonstrated for a range of stratified flows past orography^{5,6,24} and a single sphere^{3,15}, in addition to global simulations of the Earth's atmosphere employing meshes with a combination of a quasi-uniform octahedral distribution in the horizontal and prismatic spacing in the vertical²⁵. The present work provides additional comparisons with numerical and experimental results available in the literature^{17,20} for two spheres immersed in a neutrally-stratified flow, where we illustrate the scheme's efficacy together with its ability to reproduce flow intricacies generated by the presence of multiple objects. Direct Numerical Simulations (DNS) of stably-stratified flows for Froude numbers $Fr \in [0.25, \infty]$ past two spheres are also

contrasted with the previously documented computations for a single sphere³.

The remainder of the paper is organised as follows. Section II outlines the governing equations and the numerical approach employed. Section III illustrates the performance of the NFT-FV model for neutrally-stratified flows past two spheres. Section IV documents a systematic numerical study of stably-stratified flows past two spheres in representative geometrical configurations at $Re = 300$. Remarks in section V conclude the paper.

II. GOVERNING EQUATIONS AND NUMERICAL MODEL

The nonhydrostatic NFT-FV model used in this study solves the Lipps-Hemler^{26,27} anelastic system, which describes a broad class of mesoscale atmospheric flows^{5,28,29}. For a dry atmosphere, the system can be represented by the following set of conservation equations for mass, momentum, and entropy fluctuations,

$$\nabla \cdot (\mathbf{V}\bar{\rho}) = 0, \quad (1)$$

$$\frac{\partial \bar{\rho} V_I}{\partial t} + \nabla \cdot (\mathbf{V}\bar{\rho} V_I) = -\bar{\rho} \frac{\partial \phi'}{\partial x_I} + \bar{\rho} g \frac{\theta'}{\bar{\theta}} \delta_{I3} + (\nabla \cdot \boldsymbol{\tau})_I - \bar{\rho} \alpha (\mathbf{V} - \mathbf{V}_e)_I, \quad (2)$$

$$\frac{\partial \bar{\rho} \theta'}{\partial t} + \nabla \cdot (\mathbf{V}\bar{\rho} \theta') = -\bar{\rho} \mathbf{V} \cdot \nabla \theta_e - \bar{\rho} \alpha' \theta', \quad (3)$$

where x_I ($I = 1, 2, 3$) are the Cartesian coordinate directions, V_I are the corresponding components of velocity \mathbf{V} , g is the gravitational acceleration, ρ represents density, δ_{IJ} is the Kronecker delta, and $\boldsymbol{\tau}$ signifies the deviatoric stress tensor. Potential temperature is symbolised as θ and is linked to the ideal gas specific entropy, s , by $ds = c_p d \ln \theta$ (c_p is the specific heat at constant pressure). The normalised pressure perturbation, ϕ' , in equation (2) is defined as $\phi' = (p - p_e)/\bar{p}$. The density and potential temperature of the static reference state are $\bar{\rho}$ and $\bar{\theta}$ respectively, and subscripts “e” and “o” indicate the stably-stratified ambient state and constant reference values, respectively. Similarly, the potential temperature perturbation is written as $\theta' = \theta - \theta_e$, where the ambient profile, $\theta_e(x_3) = \theta_o \exp(Sx_3)$, assumes constant stratification, S . Components of deviatoric stress tensor, τ , are defined as $\tau_{IJ} = \mu \left(\frac{\partial V_I}{\partial x_J} + \frac{\partial V_J}{\partial x_I} \right)$, which incorporates the dynamic viscosity, $\mu = \bar{\rho} \nu$. The last terms in equations (2)-(3) activate wave-absorbers in the proximity of domain boundaries, with α and α' being attenuation factors for the velocity components and the potential temperature perturbation towards the ambient state³⁰.

Simulations undertaken herein focus on gravity wave dynamics for low speed atmospheric and hydrodynamic applications, for which displacements of fluid parcels are small in comparison to the scale height, S^{-1} , of the stratified environment. For such fluids, the incompressible Boussinesq limit of the anelastic system (1)-(3) is assumed, such that $\bar{\rho} = \rho_o$, $\bar{\theta} = \theta_o$, and $\theta_e(x_3) = \theta_o + Sx_3$.

Solutions are obtained using the high resolution NFT-FV model, detailed in Ref. 15. The model exploits non-oscillatory

forward-in-time integration, derived from a truncation-error analysis of uncentred two-time level approximations of an archetype inhomogeneous PDE for fluids³⁰. This semi-implicit scheme is second-order accurate and builds on the two-time-level nonlinear advection algorithm MPDATA and the corresponding solution to the elliptic Poisson equation for the pressure perturbation. Derivation of MPDATA for unstructured meshes was documented in Refs. 31 and 32. By design, MPDATA relies on an iterative application of the upwind scheme, is genuinely multidimensional and free of splitting errors. It is also conservative and sign preserving, while its monotonicity is ensured in the spirit of Flux Corrected Transport methods. A non-symmetric Krylov-subspace solver (detailed in Ref. 28) is employed to solve the Poisson equation implied by the soundproof mass-continuity constraint.

The finite volume spatial integration of the NFT-FV model adopts edge-based connectivity and operates on arbitrarily shaped polyhedral median-dual cells⁶, constructed from a given primary unstructured mesh. Such meshes are particularly suitable for simulations involving complex and multi-object geometries, and for ensuring adequate mesh resolution needed to capture key flow features, such as evolution of boundary layers and wake structure. They also facilitate MPDATA driven options for mesh adaptivity^{6,33}.

The implementation of the NFT-FV scheme for unstructured meshes embraces the distributed memory paradigm³, where efficient partitioning of the computational domain is accomplished by the MeTis library³⁴. An in-house pre-processing code configures layers of single halo points to perform MPI point-to-point communications between neighbouring partitions. These exchanges are the base of NFT-FV code parallelisation, with limited implementation of MPI global communications within the elliptic solver. The model uses a collocated arrangement for all depended variables, which simplifies the discretisation of differential operators, and has low memory and communication requirements.

A. Problem formulation

We consider flows past two identical spheres with diameter $D = 1$ located within a cuboidal computational domain. The size of the domain is dependent on the arrangement of spheres. It is chosen to maintain a minimum distance ($15D$) between any sphere and the external boundaries¹⁷, to be large enough to adequately simulate the far-wake field (cf. Ref. 3 and references therein). Geometrical configurations of the spheres adopted here follow those reported in Ref. 17 for neutrally-stratified flows. The first sphere is always placed at the origin of coordinate system $(0, 0, 0)$ and the second sphere's position is varied between simulations. For neutrally-stratified flows each geometrical configuration, illustrated in Fig. 1, is described by two parameters: the normalised gap between spheres, l/D , measured along the line connecting spheres' centres and the angle, $\theta \in [0^\circ, 90^\circ]$, this line forms with the direction of the free stream flow. In this study, with the exception of results in section IV D where we introduce a configuration tilted in the vertical plane, we focus on arrange-

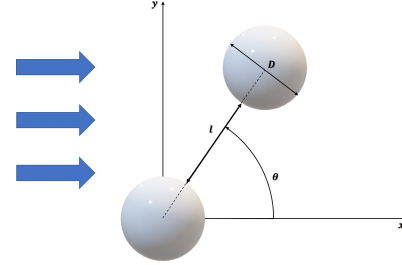


FIG. 1. Definition of the geometrical configuration of two spheres, whose centres are in the horizontal plane $z = 0$.

ments with mutual locations of spheres changed only in the horizontal plane that are most relevant to applications. The domain is therefore defined as $[-15D, 25D + (D+l)\cos\theta] \times [-15D, 15D + (D+l)\sin\theta] \times [-15D, 15D]$.

The spheres are immersed in a flow with uniform free stream velocity, $V_e = V_o = (1, 0, 0) \text{ ms}^{-1}$, prescribed at the streamwise boundaries of the domain. No-slip boundary conditions are imposed on the solid surfaces and free-slip conditions on spanwise faces of the domain. Absorbers are applied up to $2D$ from the streamwise boundaries to attenuate the solution towards ambient flow conditions, with the inverse time scales α and α' in equations (2)-(3) increasing linearly from zero at $2D$ from the domain boundary to $1/150 \text{ s}^{-1}$ at the boundary. All simulations are initialised by the solution of potential flow, then run for the non-dimensional time of $T = tV_o/D = 400$. The Reynolds and Froude numbers for a sphere with constant diameter become $Re = V_o D/\nu$ and $Fr = 2V_o/ND$ respectively. The buoyancy frequency is equal to $N = \sqrt{gS}$, where S is the constant stratification introduced in Section II.

The primary computational meshes, illustrated in Fig. 2, consist of tetrahedral elements everywhere except for 10 layers of prismatic elements with a triangular base built within $0.2D$ thick regions from the surfaces of the spheres. The prismatic layers vary in thickness, the thinnest ($0.005D$) of which are in the layer closest to the spheres. Nodes are concentrated in the near sphere regions, inter-sphere region, and in the wakes. Mesh resolution increases away from the sphere surfaces, reaching a spacing of $\sim 1D$ near to the external boundaries. Each geometric configuration has an individually generated mesh, where the number of nodes ranges between 1192456 and 1656642, with an average of ~ 1.5 million nodes. Simulations are run on 5 nodes of the Lovelace HPC cluster², each of them equipped with 40 Intel Xeon Gold 6248 CPUs. The computational domain is divided into 200 partitions and the average run-time of simulations is 18.5 hours.

The number of prismatic layers adopted results from a mesh sensitivity study performed for a stratified flow past

² <http://hpc-support.lboro.ac.uk/>

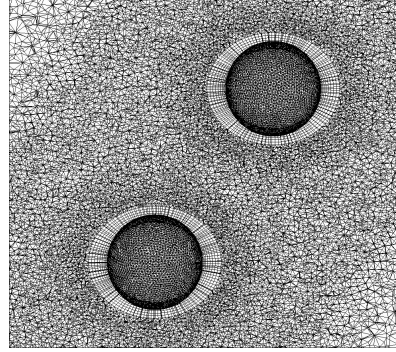


FIG. 2. A portion of the $z = 0$ cross section of primary mesh and the triangular surface meshes; geometrical configuration for $\theta = 60^\circ$ and $l/D = 1.5$.

two spheres placed in configuration $\theta = 0^\circ$ and $l/D = 1$ at $Fr = 1.667$. Two additional meshes have been defined: a coarser one with 7 prismatic layers, the thinnest of which has a thickness of $0.007D$, and a finer mesh with 13 prismatic layers with the minimum thickness of $0.004D$. The two spheres' drag coefficients (C_d) were evaluated after $T = 200$ and compared to the reference solution obtained on the computational mesh described above with 10 prismatic layers. Drag coefficients resulting from simulations employing the mesh with finer prismatic layers are similar to those computed from the current mesh, having errors relative to the reference solution $< 0.01\%$ and $< 0.1\%$ for the first and second sphere, respectively. For the mesh with coarser prismatic layers, the relative errors in the drag coefficients amount to 0.3% for both spheres.

To test the robustness of the NFT-FV scheme, white noise of amplitude $0.2V_o$ was introduced while initialising the simulation of a stratified flow past two spheres placed in the previous tandem configuration at $Fr = 1.667$. The test was then repeated with the noise amplitude increased to $2V_o$. Simulations were conducted on the computational mesh with 10 prismatic layers and resulting flows at $T = 200$ were compared with those from the non-perturbed simulation. The difference between perturbed and non-perturbed results for velocity components and potential temperature perturbation are evaluated over the entire domain and their statistics are illustrated in Table I. The low average values and standard deviations demonstrate the robustness of NFT-FV simulations which are generally run for a non-dimensional time of $T = 400$.

III. NEUTRALLY-STRATIFIED FLOW PAST TWO SPHERES

Performance of the NFT-FV model is illustrated first for neutrally-stratified flows. For computations presented in this section, the anelastic system (1)-(3) is reduced to the Navier-

TABLE I. Statistical comparison between variables of resulting flows obtained from non-perturbed and perturbed simulations. Superscript n indicates variables from perturbed simulations.

Noise	$0.2V_o$		$2V_o$	
	Average	St. deviation	Average	St. deviation
$V_1 - V_1^n$	$5.11 \cdot 10^{-4}$	$1.56 \cdot 10^{-3}$	$3.93 \cdot 10^{-4}$	$1.84 \cdot 10^{-3}$
$V_2 - V_2^n$	$3.12 \cdot 10^{-4}$	$1.15 \cdot 10^{-3}$	$2.96 \cdot 10^{-4}$	$1.31 \cdot 10^{-3}$
$V_3 - V_3^n$	$6.83 \cdot 10^{-4}$	$1.32 \cdot 10^{-3}$	$3.21 \cdot 10^{-4}$	$1.40 \cdot 10^{-3}$
$\theta' - \theta^n$	$1.35 \cdot 10^{-4}$	$3.69 \cdot 10^{-4}$	$6.47 \cdot 10^{-5}$	$3.29 \cdot 10^{-4}$

Stokes equations for incompressible isothermal flows, by omitting the entropy equation (3) and the buoyancy term in the momentum equation (2). We documented simulations of tandem configurations (i.e. $\theta = 0^\circ$) earlier in Ref. 3, whereas here parallel configurations of spheres (i.e. $\theta = 90^\circ$) with $l/D \in [0.41, 2.5]$ are selected to facilitate comparisons with the existing numerical and experimental data. Interaction between the two wakes occurs only when the spheres are in sufficient proximity, and depends on the gap between them²⁰. For the selected cases, the near-wake fields (i.e. less than $1D$ from the spheres' surfaces) are individually recognisable, as shown in Fig. 3. To aid vortex identification, Fig. 4 displays the corresponding Q-method³⁵, i.e. an instantaneous level set of the positive second invariant of the deformation tensor; $Q = 0.5(\Omega_{IJ}\Omega_{IJ} - \mathcal{D}_{IJ}\mathcal{D}_{IJ})$, where \mathcal{D}_{IJ} is half of the tensorial part of τ_{IJ} and $\Omega_{IJ} = 0.5\left(\frac{\partial V_I}{\partial x_J} - \frac{\partial V_J}{\partial x_I}\right)$ are entries of the rotation tensor.

When the spheres are closely spaced (e.g. $l/D = 0.41$, Figs. 3 and 4 upper panels) the wakes interact strongly, starting in the near wake region, merging further downstream into a non-symmetric unified wake in the horizontal plane as the vortex loops shed by each sphere become entangled. Figure 4 top-right panel demonstrates hairpin vortex shedding in the vertical plane, strongly resembling the wake induced by a single bluff body, with symmetry about the $z = 0$ plane. The resulting vortical structures are consistent with the experimental visualisation presented in Figs. 4 (a,b,c) in Ref. 20.

For $l/D = 1$, Figs. 3 and 4 middle panels, each sphere produces an identifiable individual wake in the lee, encompassing a single recirculation close to the solid surface followed by a subsequent secondary recirculation formed behind it (see Fig. 3 middle panel). The periodic shedding of vortex loops occurs simultaneously from each sphere. The loops combine downstream to form a wake almost symmetric both in the vertical and horizontal planes (cf. Fig. 4 middle panels, right and left respectively). The simulated pattern closely matches experimental observations provided by Fig. 4(d) in Ref. 20.

For $l/D = 2$, Figs. 3 and 4 lower panels, similar symmetry patterns and vortical structures emerge, however with different wake size and shedding frequency. Additionally, a single recirculation is visible in the horizontal central plane, Fig. 3, behind each sphere. In contrast, two symmetrical recirculations form in this region behind a single sphere.

For all presented cases, a history of the drag coefficient (not shown) generated by each sphere demonstrates periodic oscil-

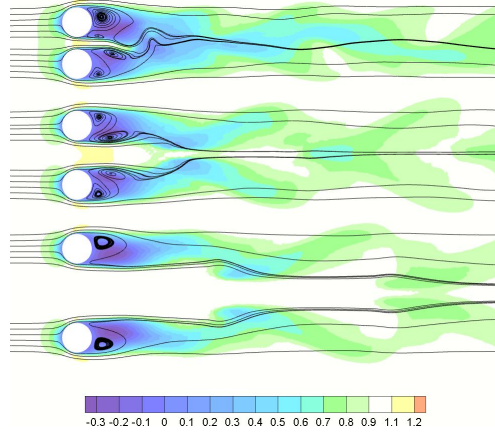


FIG. 3. Streamlines and contours of streamwise velocity component in the horizontal plane $z = 0$ for neutrally-stratified flow past spheres separated by distance of $l/D = 0.41$ (top), $l/D = 1$ (middle), and $l/D = 2$ (bottom); $Fr = \infty$.

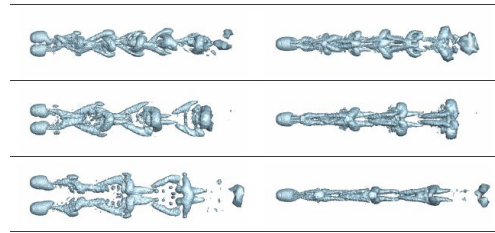


FIG. 4. Q-contours ($Q=0.04$ is used hereafter); top view (left) and side view (right) for distances between spheres $l/D = 0.41$ (top), $l/D = 1$ (middle), and $l/D = 2$ (bottom); $Fr = \infty$.

lations, attaining the same amplitude for both spheres. For the closest arrangements of spheres ($l/D < 1$) they are about half a period out of phase, while when the spheres are further apart ($l/D \geq 1.5$) the histories of the oscillations for both spheres become identical.

Figure 5 compares each sphere's normalised frequency of vortex-shedding, obtained using the NFT-FV model, with those reported in both experimental²⁰ and numerical^{17,20} studies. The vortex-shedding frequencies, f , are derived from the frequency spectra³ of the drag coefficient and are normalised by the frequency obtained for a single sphere $f_s = 0.138$. The NFT-FV simulations agree well with previous studies within the full range of selected distances, l/D .

³ Frequencies are computed using TSA v1.2 package of R software, <https://www.rdocumentation.org/packages/TSA>.

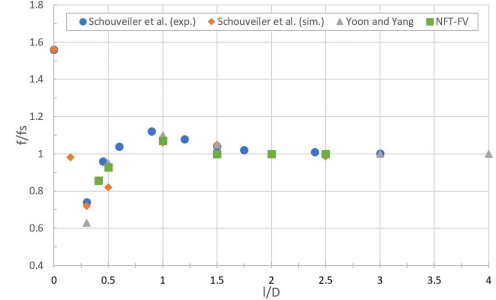


FIG. 5. Normalised vortex shedding frequency, f/f_s , as a function of the normalised gap between spheres, l/D . NFT-FV numerical results are reported together with experimental data in Ref. 20 and numerical results from Refs. 17 and 20; $Fr = \infty$.

For completeness, Table II documents the computed values of mean drag coefficient (\bar{C}_d) evaluated within the non-dimensional time interval $T = 300 - 400$. The corresponding amplitude of oscillations (C'_d), Strouhal numbers computed from the fundamental frequencies ($St = fD/V_0$), and separation angles (Φ_s) for selected simulations with $l/D \in [0.41, 2.5]$ are also provided. When the two spheres are in the parallel configuration, both spheres have matching values.

TABLE II. Overview table for simulations of neutrally-stratified flows past parallel spheres with $l/D \in [0.41, 2.5]$; parentheses indicate, if different, the value for the second sphere.

l/D	0.41	0.5	1	1.5	2	2.5
\bar{C}_d	0.742 (0.732)	0.729	0.700 (0.696)	0.682	0.674	0.669
C'_d	0.003	0.004	0.002	0.002	0.002	0.002
St	0.119	0.128	0.148	0.138	0.138	0.138
Φ_s	113	113	112	111	112	111

IV. STRATIFIED FLOW PAST TWO SPHERES

Configurations of two spheres with surface-to-surface distances $l/D \in [0.5, 1.5]$ and angles $\theta \in [0^\circ, 90^\circ]$ are selected for simulations at three stratification levels, $Fr = 1.667, 0.625, 0.25$, representative of the patterns identified in the characterisation of stratified flows past a single sphere discussed in section I. For very low stratification, the patterns are reminiscent of those obtained for neutrally-stratified flows; cf. section III and Ref. 3. For higher levels of stratification the computational results presented illustrate the most typical flow behaviour for each given flow regime. Additionally, subsection IV D provides examples of flows past tilted configurations, where the azimuthal-like angle (labelled θ') between the spheres' centres is in the vertical plane.

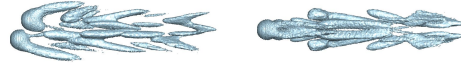


FIG. 6. Q-contours; top view (left) and side view (right) planes for $\theta = 60^\circ$ and $l/D = 0.5$; $Fr = 1.667$.

A. Weak stratification, $Fr = 1.667$

For weak stratification, features of the non-axisymmetric attached vortex regime distinguishing flow past a single sphere can also be observed when a second sphere is placed in the vicinity of the first one. However, simulations demonstrate that the proximity and relative orientation of the spheres determine the extent of wake interactions and deformations of vortices. Figure 6 illustrates a typical wake pattern obtained for the staggered configuration $\theta = 60^\circ$ and $l/D = 0.5$. Buoyancy forces, resulting from the increase of stratification, suppress the hairpin-shape vortex shedding of the neutrally-stratified flow until the flow becomes stationary, both spheres generate double wakes in the lee while the formation of gravity waves begins, as can be observed from Fig. 6.

Figure 7 shows streamlines and contours of the streamwise velocity component in the horizontal plane, $z = 0$, for parallel (upper panel), staggered (middle panel), and tandem (lower panel) configurations of the spheres. The upper panel shows simulation results with the spheres in close proximity ($l/D = 0.5$), for which significant interaction is observed. The interaction between wakes most noticeably results in their mutual flattening in the region of contact between the flows. Indeed, the interacting wake branches are most affected: their thickness is reduced, especially in the near-wake field. As a result, symmetry between the two branches of the individual wakes of each sphere is broken; however, symmetry of the entire flow about the vertical plane passing through the midpoint of the gap between spheres is present. Behind the spheres, in y - z plane flow travels towards the central plane $z = 0$ and forms two doughnut-shaped vortex rings deformed in the vertical due to stratification. These vortices, along with velocity streamwise component contours, are displayed in Fig. 8. These flows feed two recirculations that form behind the spheres in the x - z plane, not shown. For parallel configurations with distances between the spheres increased to $l/D = 1$ and $l/D = 1.5$, interactions in the far-wake field are still observed while the near-wake field of each sphere more closely resembles that of a single sphere.

For the staggered configurations (e.g. Fig. 7 middle panel), similarities between the flow behaviour behind the first sphere and that of a single sphere progressively reduce with decreasing θ . For angles $\theta \geq 45^\circ$, the majority of interactions occur in the far-wake field for $l/D = 1$ and $l/D = 1.5$; while, for $l/D = 0.5$ interactions also occur in the near-wake field affecting the shape of the internal branch of first sphere's wake, as shown in the left panel of Fig. 6. This branch is almost completely ($l/D = 0.5$) or partially ($l/D = 1$) suppressed for $\theta = 30^\circ$. The middle panel of Fig. 7 shows the latter case,

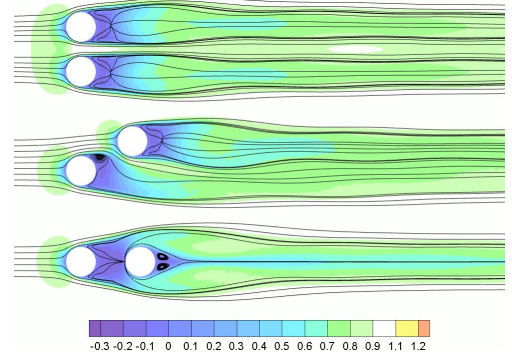


FIG. 7. Streamlines and contours of streamwise velocity component in the horizontal plane $z = 0$ for spheres placed at $\theta = 90^\circ$ and $l/D = 0.5$ (top), $\theta = 30^\circ$ and $l/D = 1$ (middle), $\theta = 0^\circ$ and $l/D = 1$ (bottom); $Fr = 1.667$.

in which the first sphere's wake is deflected allowing for a single recirculation bubble to form, while the flow pattern behind the second sphere is similar to the patterns observed in the $l/D = 0.5$ parallel configuration case discussed earlier. Finally, when the spheres are in a tandem configuration (Fig. 7 lower panel) the flow is symmetric about both the horizontal and vertical planes. Wake branches from the first sphere encompass the second sphere. The flow behind the first sphere is suppressed, forcing a flow in the y - z plane and the subsequent formation of a vortex in the region between the spheres. Its cross-section (not shown) just behind the first sphere reveals a doubly reconnected doughnut-shaped vortex, resembling that identified for a single sphere in Ref. 10 for a slightly lower Fr , with two attached vortices located horizontally indicating that the presence of the second sphere adds to the deformation induced by the stratification. However, cross sections taken close to the second sphere show the influence of the first sphere on the stagnation region, which deforms the doughnut-shaped vortex such that the two attached vortices are now placed vertically. The second sphere is shielded from the incoming free stream flow. This decreases the velocity in the gap, and consequently the local Froude and Reynolds numbers. Therefore, the flow in the gap is further suppressed by the stratification and a dividing streamline is formed, below which flow parcels are forced to travel around the second sphere. Two symmetrical recirculations can be observed in its lee in the horizontal plane, reminiscent of those typically formed in the lee-wave instability regime.

Table III reports the drag coefficients from the first and second spheres and the corresponding separation angles. Two values of separation angle are defined on the horizontal plane to address the non-symmetric geometry of the test cases. Φ_1^s is measured clockwise from the upstream centreline of each sphere to the nearest separation point; Φ_2^s is measured anticlockwise from the same direction to the nearest separation point placed on the opposite side of the sphere. When needed,

TABLE III. Overview table for simulations of stratified flows past two spheres at $Fr = 1.667$.

θ	l/D	0°			30°			45°			60°			90°		
		0.5	1	1.5	0.5	1	1.5	0.5	1	1.5	0.5	1	1.5	0.5	1	1.5
1 st sphere	C_d	0.559	0.558	0.589	0.607	0.616	0.633	0.666	0.656	0.660	0.710	0.683	0.677	0.726	0.703	0.695
	$\Phi_{s,1}^1$	105	104	106	110	108	107	145	111	110	133	115	113	113	111	110
	$\Phi_{s,1}^2$	103	103	105	102	104	106	104	105	106	109	106	105	107	107	108
2 nd sphere	C_d	0.658	0.754	0.649	0.707	0.734	0.734	0.666	0.700	0.707	0.672	0.696	0.698	0.725	0.703	0.695
	$\Phi_{s,2}^1$	137	134	122	107	110	109	105	106	106	105	106	107	106	107	108
	$\Phi_{s,2}^2$	137	133	122	127	114	108	110	108	109	105	109	110	112	113	111

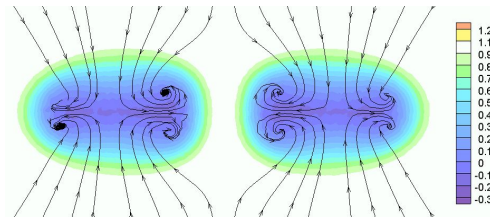


FIG. 8. Streamlines and contours of streamwise velocity component in the plane $x = 0.83$ for spheres placed at $\theta = 90^\circ$ and $l/D = 0.5$; $Fr = 1.667$. Direction of streamlines are plotted to facilitate the comprehension of flow pattern.

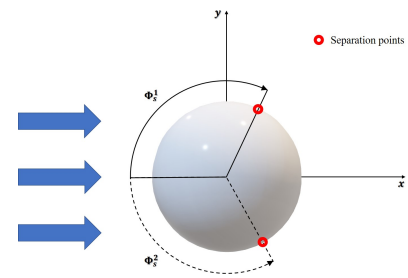


FIG. 9. Definition of the separation angles Φ_s^1 and Φ_s^2 illustrated for a single sphere.

the additional subscripts $_1$ and $_2$ are introduced to denote the first and the second sphere respectively. Figure 9 illustrates Φ_s^1 and Φ_s^2 for a single sphere placed in the centre of the domain. At the same level of stratification, the drag coefficient for a single sphere amounts to $C_d = 0.688^3$ and the horizontal separation angle is $\Phi_s^1 = \Phi_s^2 = 108^\circ$. The data is shown for all simulated geometrical configurations. For the entire range of angles and distances, the drag coefficient computed from the first sphere has the tendency to increase with θ . For low angles ($\theta < 45^\circ$) the drag coefficient for the first sphere grows as the gap between spheres increases. When the angle is increased to $\theta = 45^\circ$ results for all selected l/D become very similar, while for $\theta > 45^\circ$ the drag coefficient increases as the gap reduces. The second sphere's drag coefficient does not show a clear pattern, apart from the case of $l/D = 1$ for which the drag decreases as the angle θ increases, until it reaches an almost constant value for $\theta \geq 45^\circ$. This indicates that angle θ affects the flow solution behind second sphere more than the gap between spheres.

For all tandem configurations, the separation angle from the first sphere is always lower than that from the second one with a negligible difference between Φ_s^1 and Φ_s^2 for each sphere confirming the flow's symmetry. Notably, the separation angles computed for the first sphere nearly match that of a single sphere. For staggered and parallel configurations, the previously described flattening of internal wake branches results in general in $\Phi_{s,1}^1 > \Phi_{s,1}^2$ and $\Phi_{s,2}^2 > \Phi_{s,2}^1$. The flattening of wake branches facilitates the movement of outer separation points towards the aft of the spheres leading the separation angles $\Phi_{s,1}^1$ and $\Phi_{s,2}^2$ to be generally greater than or equal to

the single sphere's value; exceptions are $\Phi_{s,1}^1$ for configuration $\theta = 30^\circ$ and $l/D = 1.5$ and $\Phi_{s,2}^2$ for configuration $\theta = 60^\circ$ and $l/D = 0.5$. For some configurations of close proximity spheres ($l/D = 0.5$), the spread between values of Φ_s^1 and Φ_s^2 (for either sphere) is larger. In such cases, a recirculation bubble is formed behind the first sphere, similar to that seen in Fig. 7 middle panel, but with its centre shifted towards the sphere's centreline; leading to an increased separation angle, $\Phi_{s,1}^2$. In the parallel configuration (Fig. 7 upper panel), the flattening of wake branches is associated with $\Phi_{s,1}^1 \sim \Phi_{s,2}^2$ and $\Phi_{s,1}^2 \sim \Phi_{s,2}^1$.

B. Medium stratification, $Fr = 0.625$

At medium stratification, flow impinging on a single sphere results in a so-called steady-state lee-wave instability regime. The resulting flow for two staggered spheres is illustrated using the Q-method in Fig. 10. The flows behind each sphere reach steady states that have similar features to those reported in Ref. 3 for a single sphere. Well developed gravity waves can be seen in the lee, strongly interacting with the wakes from both spheres.

The streamwise velocity component plots with associated streamlines in Fig. 11 illustrate the effects of increased stratification for configurations similar to those examined in Fig. 7. In all cases fluid parcels contained below the height of dividing streamline, as discussed in Ref. 15, flow around the

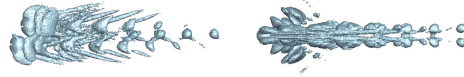


FIG. 10. Q-contours; top view (left) and side view (right) for $\theta = 60^\circ$ and $l/D = 0.5$; $Fr = 0.625$.

spheres forming leeward recirculation bubbles. For the parallel configuration (Fig. 11 upper panel), the pattern is almost symmetric about the vertical plane of mesh symmetry between the two spheres (i.e. $y = 0.75$) and only one recirculation is visible in the horizontal ($z = 0$) plane behind each sphere, with the second one being suppressed. Aided by the recirculations, the flow accelerates through the gap between spheres to create a region of locally increased velocity which soon decreases further downstream.

The symmetry noted for the parallel configuration is not present for staggered configurations (Fig. 11 middle panel). The two attached recirculations formed behind each sphere are distorted by the deflection and interaction between the wakes. In the tandem configuration (Fig. 11 lower panel), planar symmetry is present and the two recirculations behind the second sphere are similar to those obtained for a single sphere at $Fr = 0.625$, however the recirculations behind the first sphere are suppressed and, therefore, much smaller.

Lee-wave crest instability and overturning are induced by a strong vertical shear. Tiny recirculations, representing overturning motions of fluid parcels, are illustrated for the tandem configuration in the vertical plane ($y = 0$) in Fig. 12. These recirculations result from the combined effects of buoyancy and shear¹⁰, leading to the name “lee-wave instability regime”. Only flow parcels above the dividing streamline have sufficient kinetic energy to flow over the top of the spheres. The associated buoyancy-induced gravity waves radiating in the lee of both spheres are presented in the vorticity plot in Fig. 13 for a tandem configuration, along with the results achieved for a single sphere. Gravity waves are shown to propagate in proximity to the first sphere; however, the wave amplitudes start to differ downstream of the second sphere. In Fig. 13 upper panel, regions of high and low amplitudes of the absolute value of vorticity display positions of constructive and destructive interferences, respectively. This interference pattern develops conically immediately behind the spheres, with a cone angle of $\sim 55^\circ$ from the flow direction. In this region the first destructive interference is noticeable, until eventually the waves dissipate downstream. Similar interference patterns are also observed for staggered configurations (not shown). The superposition pattern is induced by the presence of the second sphere, while lee-wave behaviour is more consistent with the pattern of a single sphere. The geometry of the configuration drives the interference influencing frequency, maximum vorticity amplitude, and the shape of the resulting lee waves.

Finally, we record that the flow solution for the tandem configuration and distance $l/D = 1$ is a special case, which displays periodic horizontal oscillations in the far-wake field, as shown in Fig. 14. The same behaviour is not noted for other

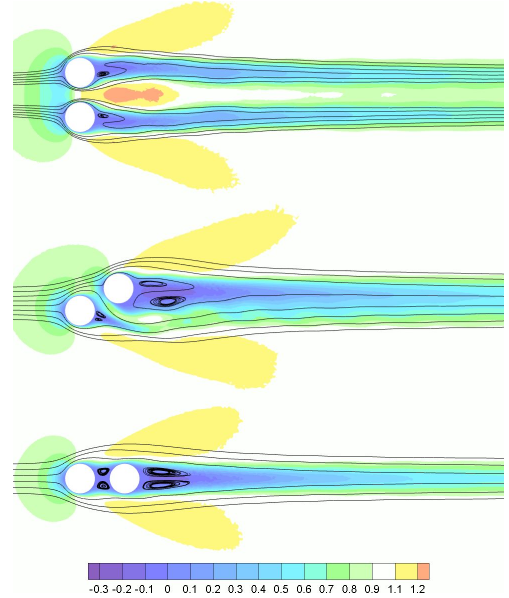


FIG. 11. Streamlines and contours of streamwise velocity component in the horizontal plane $z = 0$ for spheres placed at $\theta = 90^\circ$ and $l/D = 0.5$ (top), $\theta = 30^\circ$ and $l/D = 0.5$ (middle), $\theta = 0^\circ$ and $l/D = 0.5$ (bottom); $Fr = 0.625$.

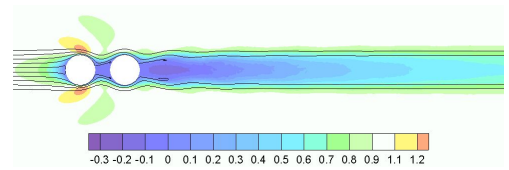


FIG. 12. Streamlines and contours of streamwise velocity component in the vertical plane $y = 0$ for spheres in a tandem configuration and $l/D = 0.5$; $Fr = 0.625$.

values of l/D , where steady state is maintained (e.g. configuration $\theta = 0^\circ$ and $l/D = 0.5$ in the lower panel of Fig. 11). Notably, for *neutrally*-stratified flows at $Re = 250$, varying the distance between spheres placed in a tandem arrangement also displays a range of flow regimes: from planar steady state to periodic flow³⁶.

Lee waves trapped between ridges have been studied in Ref. 2 for elongated obstacles positioned perpendicular to the flow direction. Despite the differences between simulations of stratified flow past spheres and atmospheric flows over mountain ridges, the number of lee-wave crests across the gap between obstacles display a resemblance. Present results agree with the observation that trapped lee waves increase in num-

TABLE IV. Overview table for simulations of stratified flows past two spheres at $Fr = 0.625$.

θ	l/D	0°			30°			45°			60°			90°		
		0.5	1	1.5	0.5	1	1.5	0.5	1	1.5	0.5	1	1.5	0.5	1	1.5
1 st sphere	C_d	1.078	1.078	1.074	1.167	1.164	1.164	1.255	1.215	1.210	1.344	1.278	1.254	1.422	1.348	1.310
	$\Phi_{s,1}^1$	136	137	134	175	150	147	172	156	151	167	158	154	158	157	153
	$\Phi_{s,1}^2$	138	134	136	140	137	178	136	136	139	136	138	140	139	141	143
2 nd sphere	C_d	0.311	0.474	0.490	0.988	1.100	1.194	1.219	1.255	1.286	1.321	1.328	1.325	1.422	1.351	1.313
	$\Phi_{s,2}^1$	129	127	122	147	149	150	147	148	145	142	144	143	141	141	143
	$\Phi_{s,2}^2$	129	127	122	87	135	138	129	138	145	142	147	151	158	154	154

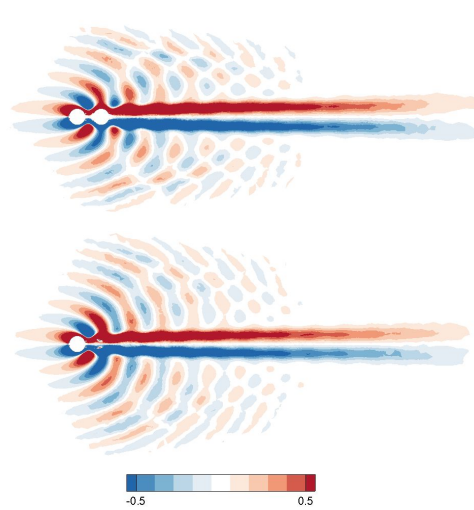


FIG. 13. Contours of instantaneous vorticity component normal to the central vertical plane, $y = 0$, for flow past two spheres placed at $\theta = 0^\circ$ and $l/D = 0.5$ (top) and flow past a single sphere (bottom); $Fr = 0.625$.

ber as the gap between obstacles increases.

Table IV documents drag coefficients from the first and second spheres, along with the corresponding separation angles. For reference, at the same stratification level the single sphere value of drag coefficient is $C_d = 1.230^3$ and separation angle is $\Phi_s^1 = \Phi_s^2 = 144^\circ$. Similarly as for a low stratification described above, the presence of a second sphere can affect these values. For $\theta = 0^\circ$, the second sphere is partially shielded from the incoming flow by the first one, therefore, drag coefficient of the second sphere is substantially smaller, but tends to grow with the increase of gap between spheres. As the angle increases to $\theta = 30^\circ$, the drag coefficient slightly increases for the first sphere and dramatically for the second which is now more exposed to the incoming flow. This growth is more pronounced as the gap between spheres increases. In fact, for $l/D = 1.5$ the drag coefficient computed for the second sphere is even higher than for the first one. An increase

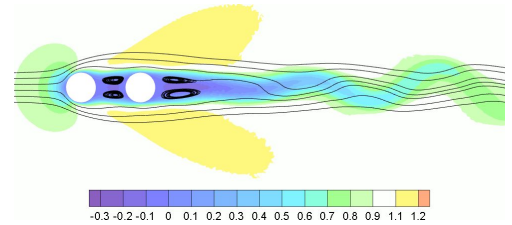


FIG. 14. Streamlines and contours of streamwise velocity component in the horizontal plane $z = 0$ for spheres in a tandem configuration and $l/D = 1$; $Fr = 0.625$.

of the second sphere's drag coefficient continues within the interval $30^\circ < \theta \leq 60^\circ$. Although the rate of increase is lower than rates observed for the lower values of θ , the drag from the second sphere is larger than that of the first one, even for the distance $l/D = 1$. When $\theta = 60^\circ$, values of the second sphere's drag coefficient are (almost) the same for all considered gaps between spheres. Finally, when spheres are placed in the parallel configuration, a difference between drag coefficients computed for both spheres is less than 1%, suggesting that their mutual interference is weak.

The separation angle $\Phi_{s,1}^1$ remains close to $\Phi_{s,2}^2$, and $\Phi_{s,1}^2$ has similar values to $\Phi_{s,2}^1$ for parallel configuration of spheres, alike that observed for low stratification. Moreover, the pattern of separation angles for which $\Phi_{s,1}^1$ and $\Phi_{s,2}^2$, respectively, are higher than $\Phi_{s,1}^2$ and $\Phi_{s,2}^1$ is still apparent when $\theta = 90^\circ$. These observations can only be partially extended to the staggered configurations. In fact, the same trend in separation angles is observed for the first sphere in the majority of cases, i.e. $\Phi_{s,1}^1 > \Phi_{s,1}^2$, while for the second sphere there is no clear tendency. For the tandem configurations, values of Φ_s^1 and Φ_s^2 differ by less than 3° . This suggests that equal portions of flow circumnavigate the spheres in the two possible directions. Furthermore, for $\theta = 0^\circ$ the separation angles for the first sphere are greater than those for the second one and all of them are lower than the separation angle for a single sphere. For staggered configurations in which the spheres are close to each other, e.g. $\theta = 30^\circ$ and $l/D = 0.5$ (reported in middle panel of Fig. 11), the second sphere can force the closest portion of the flow which circumnavigates the first sphere to delay the flow separation leading to an in-

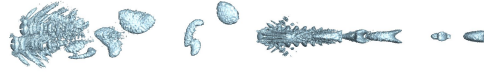


FIG. 15. Q-contours; top view (left) and side view (right) for $\theta = 60^\circ$ and $l/D = 0.5$; $Fr = 0.25$.

crease of the corresponding separation angle; in this particular case its value is $\Phi_{s,1}^1 = 175^\circ$. The flow deflection is associated with the low separation angle measured on the second sphere, i.e. $\Phi_{s,2}^2 = 87^\circ$.

C. Strong stratification, $Fr = 0.25$

A flow past a single sphere at $Fr = 0.25$ is characterised by the well-documented two-dimensional vortex shedding regime. Fig. 15 shows a three-dimensional representation of the flow past two spheres placed in a staggered configuration with $\theta = 60^\circ$ and $l/D = 0.5$. Shapes of vortex structures in the near-wake field of each sphere are comparable with those for a single sphere reported in Ref. 3. The far-wake field however, although still periodic, differs greatly due to the presence of the second sphere. The interaction between the wakes of each sphere also results in different frequencies of lee waves and vortex shedding (Fig. 15 right panel) in comparison to flows past a single sphere. The corresponding Strouhal numbers⁴ are listed in Table V and will be discussed later.

The generation and development of vortices, that are shed behind the two spheres, depends strongly on their configuration. Periodic behaviour for the tandem configuration with $l/D = 0.5$ is illustrated in Fig. 16, displaying instantaneous streamlines and streamwise velocity component contours. The figure also shows how extended shear layers, generated by the first sphere, encapsulate the near-wake field inhibiting vortex development. This is also reflected in the almost constant values of drag coefficients, computed for both spheres, with the maximum amplitude of drag coefficients over their periodic histories not exceeding 1% of \bar{C}_d . The described flow pattern occurs for all simulated tandem configurations at $Fr = 0.25$.

Figure 17 presents streamlines and contours of streamwise velocity component in the horizontal plane ($z = 0$) for a further three representative cases, organised according to angle θ . For staggered configurations (Fig. 17 top and middle panels), some periodicity of the flow in the near-wake field is restored. Figure 17 upper panel (configuration with $\theta = 30^\circ$ and $l/D = 0.5$) demonstrates that the merging of wakes in the near-wake field determines the same Strouhal number for both spheres. Altering the staggered configuration such that the second sphere is no longer directly behind the first (e.g. $\theta = 60^\circ$ and $l/D = 1$, Fig. 17 middle panel), the presence of

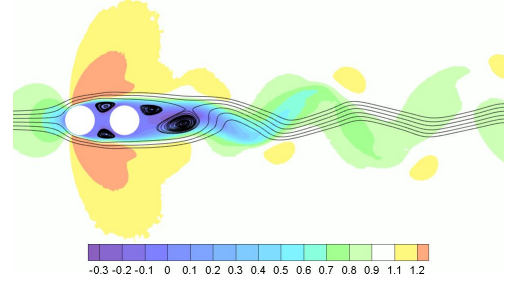


FIG. 16. Streamlines and contours of streamwise velocity component in the horizontal plane $z = 0$ for spheres in a tandem configuration with $l/D = 0.5$; $Fr = 0.25$.

shear layers in the gap and separate recirculations attached to the spheres trigger wake unification in the far-wake field. The pattern in this case results in multiple vortex shedding frequencies. Table V displays the Strouhal numbers computed from the two highest frequency peaks for the first sphere, while those for the second sphere are not readable from the spectral analysis. Figure 17 lower panel shows the flow for a parallel configuration with $l/D = 1.5$. The wakes remain separate in the near-wake field, evoking the same values of drag coefficient and Strouhal numbers for both spheres. They merge gently further downstream.

Figure 18, displaying the y-component of instantaneous vorticity in central vertical plane ($y = 0$), shows characteristics of the lee-wave pattern demonstrating constructive and destructive interferences. Strong stratification facilitates a pronounced lee-wave propagation upstream and a fast wave dissipation downstream. Furthermore, both a higher frequency of lee waves and reduced area of the interference pattern are observed in comparison to the medium stratification case in upper panel of Fig. 13. Moreover, the displayed vorticity component shows periodic features in the far-wake field which are symmetric about the centreline of wake. These represent the downstream vortices, also visible in the three-dimensional Q-plots in Fig. 18, for a staggered configuration. Such wake features are also observed for a flow past a single sphere at the same stratification³.

Table V provides quantitative data obtained from the simulations. The mean drag coefficient \bar{C}_d was evaluated within the non-dimensional time interval $T = 300 - 400$ with the corresponding amplitude, C_d' , while the Strouhal numbers, St , are computed based on the two dominant frequencies of each drag coefficient spectrum. Additionally, the table provides the values of separation angles Φ_s (previously defined). For reference, the values for a flow past a single sphere at $Fr = 0.25$ are $\bar{C}_d = 1.617$ with amplitude $C_d' = 0.01$, $St = 0.375$, and $\Phi_s^1 \approx \Phi_s^2 \approx 99^\circ$. The overall patterns of \bar{C}_d for both spheres are similar to those obtained for medium stratification ($Fr = 0.625$), however, there are some notable differences. In particular, the growth of drag coefficient computed for the first sphere for increasing θ is now not as smooth. Values of \bar{C}_d

⁴ The definition of Strouhal number (cf. section IV) is applied adopting the first two frequencies resulting from the spectrum of drag coefficient.

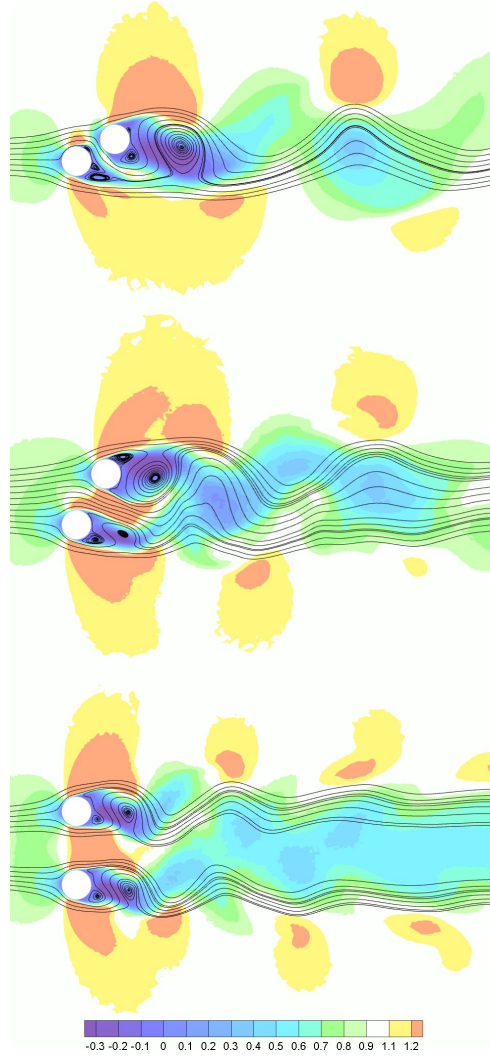


FIG. 17. Streamlines and contours of streamwise velocity component in the horizontal plane $z = 0$ for spheres placed at $\theta = 30^\circ$ and $l/D = 0.5$ (top), $\theta = 60^\circ$ and $l/D = 1$ (middle), $\theta = 90^\circ$ and $l/D = 1.5$ (bottom); $Fr = 0.25$.

remain constant for all l/D when $\theta \leq 30^\circ$ and then increase for 45° . Further increases of \bar{C}_d are moderate with the exception of $l/D = 1$ case, for which \bar{C}_d increases noticeably for $\theta \geq 60^\circ$. Moreover, for the tandem and parallel configurations the first sphere's drag coefficients, normalised by \bar{C}_d from the single sphere, have similar values to the normalised drag co-

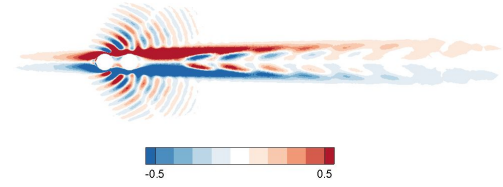


FIG. 18. Contours of instantaneous vorticity component normal to the central vertical plane, $y = 0$, for flow past two spheres placed at $\theta = 0^\circ$ and $l/D = 0.5$; $Fr = 0.25$.

efficients computed for medium stratification ($Fr = 0.625$). This demonstrates their relative independence from stratification. Drag coefficients computed from the second sphere have negative values for all tandem configurations, showing that the established flow induces a forcing which would tow the object towards the first sphere. After increasing angle θ , the second sphere's drag coefficient approaches a value similar to that computed for a single sphere and exceeds it at approximately $\theta = 60^\circ$, for all considered distances l/D , with a tendency to increase as the gap increases.

Interpretation of resulting patterns is aided by the Strouhal number, computed from the history of \bar{C}_d , therefore we evaluate St tendencies displayed in Table V further. For tandem configurations the flow reaches steady state, hence the Strouhal number is not computed. When the angle between spheres is increased, for $0 < \theta \leq 45^\circ$, a single dominant frequency is observed for the first sphere and multiples of this single dominant frequency are also detectable for the second sphere. The values of St_1 are the same for both spheres, outlining the unification of flow patterns (as previously discussed). The configuration $\theta = 45^\circ$ and $l/D = 1.5$ shows features which are characteristic for higher angles between spheres, middle panel of Fig. 17, consisting of multiple vortex shedding frequencies behind at least one sphere; however, the same values of St_1 are found for each of the two spheres. This indicates that the vortex shedding follows an overall fundamental period. Some exceptions are noted, especially for the parallel configuration, in which clear predominant frequencies cannot be detected, since the \bar{C}_d harmonics are highly superimposed. However, when the two spheres are widely separated (e.g. $l/D = 1.5$, lower panel of Fig. 17) the independence of flows behind each sphere results in the same Strouhal numbers, as expected. Moreover, in general, for the same θ the Strouhal number increases with l/D ; this pattern is more pronounced for lower values of θ .

Table V also shows that separation angles for strong stratification are lower in comparison with those for medium stratification, where their values approach the maximum, cf. Ref. 10 for a single sphere. Separation angles for the parallel configuration $\Phi_{s,1}^2$ and $\Phi_{s,2}^1$ are close to the Φ_s^1 and Φ_s^2 values for a single sphere. For lower angles θ , computations from the first sphere display the tendency of $\Phi_{s,1}^1$ to decrease with increased values of θ and l/D ; in particular, as $\theta \searrow 0^\circ$ val-

TABLE V. Overview table for simulations of stratified flows past two spheres at $Fr = 0.25$. Symbols are adopted to convey different alternatives for Strouhal number: — indicates that no Strouhal number can be computed (i.e. steady flow), asterisk * denotes that a well-defined value is not observed, NV (i.e. not visible) implies that the frequency peak defining the St is not distinguishable, and brackets including St_2 designate that the value is double of fundamental St_1 .

	θ	0°			30°			45°			60°			90°		
	l/D	0.5	1	1.5	0.5	1	1.5	0.5	1	1.5	0.5	1	1.5	0.5	1	1.5
1 st sphere	C_d	1.394	1.358	1.328	1.414	1.377	1.358	1.545	1.445	1.445	1.675	1.624	1.696	1.728	1.853	1.834
	C_d'	< 0.001	< 0.001	< 0.001	0.05	0.03	0.01	0.05	0.02	0.01	0.03	0.03	0.04	0.08	0.08	0.03
	St_1	—	—	—	0.119	0.128	0.138	0.109	0.128	0.138	0.109	0.277	0.237	*	*	0.198
	St_2	—	—	—	NV	NV	NV	NV	NV	0.247	NV	0.128	0.148			(0.395)
	$\Phi_{s,1}^1$	101	100	98	106	104	101	160	111	105	144	123	113	116	115	110
	$\Phi_{s,1}^2$	100	96	99	96	94	96	94	95	95	92	96	99	89	99	99
2 nd sphere	C_d	-0.155	-0.142	-0.088	1.385	1.450	1.502	1.502	1.589	1.620	1.576	1.632	1.642	1.683	1.670	1.836
	C_d'	< 0.001	< 0.001	< 0.001	0.08	0.05	0.04	0.05	0.03	0.03	0.02	0.04	0.04	0.1	0.08	0.03
	St_1	—	—	—	0.119	0.128	0.138	0.109	0.128	*	0.109	*	0.237	*	*	0.198
	St_2	—	—	—	(0.237)	(0.247)	(0.267)	(0.217)	(0.267)		0.207		0.089			(0.395)
	$\Phi_{s,2}^1$	111	113	126	98	97	101	91	98	99	148	88	101	89	95	95
	$\Phi_{s,2}^2$	106	118	122	62	114	139	79	84	89	126	87	95	119	116	115



FIG. 19. Q-contours; top view (left) and side view (right) for a tilted configuration with $\theta' = 30^\circ$ and $l/D = 0.5$; $Fr = 1.667$.

ues of $\Phi_{s,1}^1$ become closer to that of a single sphere. Separation angles $\Phi_{s,1}^2$ are more established than $\Phi_{s,1}^1$ and their values are always close to that of a single sphere (although mostly slightly lower). On the other hand, computations of separation angles for the second sphere show greater variability than for the first one; such variability is observed especially for $\Phi_{s,2}^2$, since a trend of $\Phi_{s,2}^1$ to increase with l/D is noticeable for some angles θ .

D. Second sphere tilted in the vertical plane

A further class of configurations can be established by introducing an azimuthal-like angle θ' , defined in the x - z plane counter-clockwise from the x -axis to the line connecting spheres' centres. This configuration is analogous to the picture in Fig. 1, replacing y and θ with z and θ' , and the spheres' centres now remaining in the x - z plane. Accordingly, the domain is now defined as $[-15D, 25D + (D + l) \cos \theta'] \times [-15D, 15D] \times [-15D, 15D + (D + l) \sin \theta']$ and contains 1301424 mesh nodes. To illustrate the flow resulting from these tilted configurations⁵, simulations of stratified flows past two spheres at $Fr = 1.667$, $Fr = 0.625$, and $Fr = 0.25$ are documented for configurations described by $\theta' = 30^\circ$ and $l/D = 0.5$.

⁵ The spheres appear directly behind each other in the horizontal, but are staggered in the vertical such that the second is either above or below the central horizontal plane ($z = 0$).

Figure 19 shows the Q-plots for weak stratification, i.e. $Fr = 1.667$. The characteristics of the non-axisymmetric attached vortex regime are present, with the double wake structure visible in the horizontal plane (left panel) and recirculations behind the spheres detected in the x - z plane (not shown). The doughnut-shaped vortices are still visible in the lee of both spheres, however they are distorted in the vertical not only by stratification but also due to compression generated as the flow interacts with the spheres. The absence of the dividing streamline for weak stratification enables the entire flow impacting the first sphere to pass either above or underneath it, depending on the hemisphere encountered. The fluid parcels which rise over the top of the first sphere then pass below the second one forming the shear layer between the spheres which merges with a shear layer inherently generated by the second sphere. The tilted configuration with $\theta' = 30^\circ$ facilitates the constructive interference of lee waves generated from the two spheres, as the lee waves in Fig. 19 are more evident than those in Fig. 6 especially in the far-wake field. Drag coefficients of first and second sphere placed in this arrangement are $C_d = 0.679$ and $C_d = 0.665$, respectively.

For medium stratification ($Fr = 0.625$), the resulting flow for tilted configurations becomes unsteady and shows all the characteristics of the two-dimensional vortex shedding regime identified for flows past a single sphere at higher stratification levels; evidenced by Q-plots in Fig. 20 where the key features from Fig. 15 can be found. The wake behind the spheres is primarily defined by the interaction of fluid parcels which circumnavigate both spheres. The far-wake field shows a merged wake, characterised by vortices shed by the two spheres. The near-wake field in the two horizontal planes, each coinciding with the centre of a sphere, have two non-symmetric recirculations behind the first sphere and one in the lee of the second (not shown). For $\theta' = 30^\circ$, the fluid parcels below the lower dividing streamline of the first sphere can pass underneath it, however the parcels above the upper dividing streamline of the first sphere, after passing over its top, are forced to flow



FIG. 20. Q-contours; top view (left) and side view (right) for a tilted configuration with $\theta' = 30^\circ$ and $l/D = 0.5$; $Fr = 0.625$.

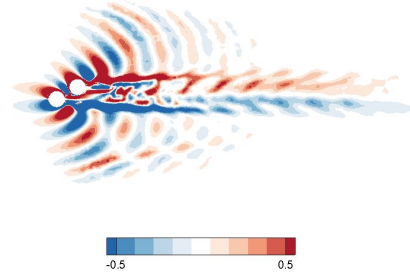


FIG. 21. Contours of instantaneous vorticity component normal to the central vertical plane, $y = 0$, for flow past two spheres placed in a tilted configuration with $\theta' = 30^\circ$ and $l/D = 0.5$; $Fr = 0.625$.

around the second sphere, due to insufficient kinetic energy. The parcels above the upper dividing line of the second sphere can rise over its top, while the majority of remaining parcels have lower kinetic energy and travel around the sphere; although a small number of parcels pass through the gap and under the second sphere, their motion is inhibited by parcels with opposing velocities coming from recirculations formed behind both spheres. The overturning of first lee-wave crest is still visible and the lee-wave pattern is shown in Fig. 21, where the y -component of vorticity is displayed. Downstream of both spheres, amplitudes of lee waves from the spheres predominantly sum (e.g. interfere constructively) in the half-plane described by $y = 0, z > 0$; while, where $y = 0, z < 0$ destructive interferences of lee waves also contribute, forming a pattern similar to that in lower panel of Fig. 13 which dissipates quickly downstream. Vortices in the near-wake field are distorted owing to wake interactions. These patterns indicate that the downstream flow is reminiscent of a flow past a single bluff body elongated in the direction perpendicular to the free stream flow. This effectively decreases the Froude number for this configuration, accounting for similarities of flow structures with those of strongly stratified flows past an isolated sphere in the two-dimensional vortex shedding regime.

For the tilted configuration displayed and medium stratification, drag coefficients and related amplitudes averaged over the interval $T = 300 - 400$ are $\bar{C}_d = 1.312$ and $C'_d = 0.015$ for the first sphere and $\bar{C}_d = 1.189$ and $C'_d = 0.036$ for the second one.

Figure 22 left panel displays the top view of the three-dimensional representation for stratified flow with strong stratification ($Fr = 0.25$). The near-wake field shows the same main characteristics as those observed in Fig. 15, while the far-wake field clearly demonstrates the two-dimensional pe-

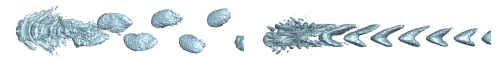


FIG. 22. Q-contours; top view (left) and side view (right) for a tilted configuration with $\theta' = 30^\circ$ and $l/D = 0.5$; $Fr = 0.25$.

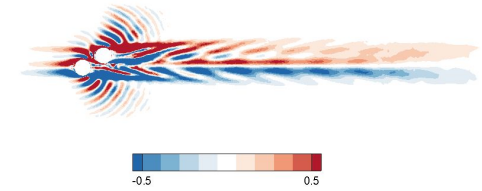


FIG. 23. Contours of instantaneous vorticity component normal to the central vertical plane, $y = 0$, for flow past two spheres placed in a tilted configuration with $\theta' = 30^\circ$ and $l/D = 0.5$; $Fr = 0.25$.

riodic vortex shedding of the flow which resembles that of a single sphere, cf. Ref. 3. At this stratification, the dividing streamline height increases towards higher (and lower) z -coordinates facilitating the planar development of the flow and confining the lee-wave spreading, this confirms the findings from previously studied configurations. Figure 23 displays the y -component of vorticity. Despite differences in the near-wake field and the absence of destructive interferences downstream, the main flow features displayed in Fig. 18 are also present in this simulation; demonstrating the predominance of stratification in defining the flow patterns also for tilted configurations of spheres. As before, this configuration resembles a single vertically elongated bluff body – effectively decreasing the Froude number.

For the tilted configuration with $\theta' = 30^\circ$ and strong stratification, the drag coefficient and corresponding amplitude averaged over the interval $T = 300 - 400$ are $\bar{C}_d = 1.601$ and $C'_d = 0.013$ for the first sphere and $\bar{C}_d = 1.189$ and $C'_d = 0.015$ for the second one.

V. CONCLUSIONS

This numerical study investigates stratified flows past two identical spheres at $Re = 300$ over a selection of representative configurations. For flows past a single sphere, the experimental and numerical characterisations identified three dominant flow regimes named: a non-axisymmetric attached vortex for weak-, lee-wave instability for medium-, and two-dimensional vortex shedding for strong-stratification. For flows past two spheres these three dominant regimes can still be used for the overall characterisation of the main tendencies in flow behaviour, however, within these regimes the interference between the flows and the spheres results in numerous variations of structures.

For weak stratification, $Fr = 1.667$, the wakes behind two spheres are suppressed by the buoyancy forcing and the flow

reaches steady state, similarly as for a single sphere. A combination of the buoyancy driven vertical deformation and the flow interactions due to the presence of the spheres result in the creation of doughnut-shaped attached vortex structures which also appear in flows behind a single sphere. The gravity waves radiation begins from both spheres in an analogous way to the single sphere case.

As the stratification increases, gravity waves become more pronounced and their amplitude tends to reach the maximum at $Fr \approx 1$, similarly as for a single sphere. For the cases illustrated here at $Fr = 0.625$, the structures and mechanisms of the single sphere lee-wave instability flow regime are also present; however, some of the two recirculations which would appear behind a single sphere in the horizontal central plane are suppressed by the interactions resulting from the presence of two spheres. Tiny recirculations due to lee-wave instability can be observed in the vertical central plane ($y = 0$) behind the two spheres. The amplitudes of the gravity waves are substantially different when two spheres are present since the waves generated by each sphere contribute to construction or destruction of the gravity waves induced by the other sphere.

For the stronger stratification, the flow pattern demonstrates two-dimensional vortex shedding set in the horizontal plane, matching behaviour observed for a single sphere. The characteristic feature of this regime is fluid parcels travelling around the spheres and producing a periodic motion analogous to that observed for flows past cylinders. The gravity wave interference patterns are still present albeit in a reduced form and generally the waves dissipate downstream sooner than for medium stratification.

Simulations performed with the second sphere behind but tilted in the vertical with respect to the first sphere show how specific configurations of spheres can trigger a flow similar to the flow past a single vertically elongated bluff body, consequently these simulations result in flows which would typically be expected at higher stratification and bare similarities to cases of hypothetical hills with different heights, cf. Ref. 2. Formation of such patterns is highly dependent on the azimuthal-like angle θ' and the distance between spheres.

In studies of flows past a single sphere⁴ qualitative agreement was found in DNS and DES simulation results at the same Froude but different Reynolds numbers. It is likely that the same is true for flows past configurations of two spheres, making the presented study also useful for larger Reynolds numbers. Additionally, we note that the NFT-FV computations, for a neutrally-stratified flow past two spheres in the parallel configuration, agree very well with experimental tests reported in Ref. 20 and improve on the numerical results presented there. This validation, together with validations of the NFT-FV model for the stratified flows past a single sphere in Ref. 3, boost our confidence in the accuracy of results obtained in this study.

ACKNOWLEDGMENTS

This work was supported in part by the funding received from the EPSRC studentship grant 1965773, and Horizon

2020 Research and Innovation Programme (ESCAPE2 grant agreement no. 800897).

DATA AVAILABILITY

The data that support the findings of this study are available from the corresponding author upon reasonable request.

REFERENCES

- ¹J. T. Lee, R. E. Lawson Jr., and G. L. Marsh, "Flow visualisation experiments on stably stratified flow over ridges and valleys," *Meteorol. Atmos. Phys.* **37**, 183–194 (1987).
- ²V. Grubišić and I. Stiperski, "Lee-wave resonances over double bell-shaped obstacles," *J. Atmos. Sci.* **66**, 1205–1228 (2009).
- ³F. Cocetta, M. Gillard, J. Szmelter, and P. K. Smolarkiewicz, "Stratified flow past a sphere at moderate Reynolds numbers," *Comput. and Fluids* (under review), available at <http://arxiv.org/abs/2101.06807>.
- ⁴T. S. Orr, J. A. Domaradzki, G. R. Spedding, and G. S. Constantinescu, "Numerical simulations of the near wake of a sphere moving in a steady, horizontal motion through a linearly stratified fluid at $Re=1000$," *Phys. Fluids* **27**, 035113 (2015).
- ⁵P. K. Smolarkiewicz, J. Szmelter, and A. A. Wyszogrodzki, "An unstructured-mesh atmospheric model for nonhydrostatic dynamics," *J. Comput. Phys.* **254**, 184–199 (2013).
- ⁶J. Szmelter, Z. Zhang, and P. K. Smolarkiewicz, "An unstructured-mesh atmospheric model for nonhydrostatic dynamics: towards optimal mesh resolution," *J. Comput. Phys.* **294**, 363–381 (2015).
- ⁷T. Bodnár and P. Fraunié, "Numerical simulation of three-dimensional lee waves behind an isolated hill," *Appl. Math. Model.* **78**, 648–664 (2020).
- ⁸A. Warn-Varnas, J. Hawkins, P. K. Smolarkiewicz, S. A. Chin-Bing, D. King, and Z. Hallock, "Solitary wave effects North of Strait of Messina," *Ocean Modelling* **18**, 97–121 (2007).
- ⁹M. Esmailpour, J. E. Martin, and P. M. Carrica, "Near-field flow of submarines and ships advancing in a stable stratified fluid," *Ocean Eng.* **123**, 75–95 (2016).
- ¹⁰Q. Lin, W. R. Lindberg, D. L. Boyer, and H. J. S. Fernando, "Stratified flow past a sphere," *J. Fluid Mech.* **240**, 315–354 (1992).
- ¹¹J. M. Chomaz, P. Bonneton, and E. J. Hopfinger, "The structure of the near wake of a sphere moving horizontally in a stratified fluid," *J. Fluid Mech.* **254**, 1–21 (1993).
- ¹²S. Nidhan, J. L. Ortiz-Tarin, K. Chongsiripinyo, S. Sarkar, and P. J. Schmid, "Dynamic mode decomposition of stratified wakes," in *AIAA Aviation 2019 Forum* (2019) doi: 10.2514/6.2019-3330.
- ¹³Q. Zhou and P. J. Diamessis, "Large-scale characteristics of stratified wake turbulence at varying Reynolds number," *Phys. Rev. Fluids* **4**, 084802 (2019).
- ¹⁴V. A. Gushchin and P. V. Matyushin, "Simulation and study of stratified flows around finite bodies," *Comput. Math. Math. Phys.* **56**, 1034–1047 (2016).
- ¹⁵J. Szmelter, P. K. Smolarkiewicz, Z. Zhang, and Z. X. Cao, "Non-oscillatory forward-in-time integrators for viscous incompressible flows past a sphere," *J. Comput. Phys.* **386**, 365–383 (2019).
- ¹⁶F. Cocetta, M. Gillard, and J. Szmelter, "Numerical characterisation of stably stratified flows past spheres," in *figshare* (2020) doi: <https://doi.org/10.17028/rd.1boro.12095997.v1>.
- ¹⁷D. H. Yoon and K. S. Yang, "Characterization of flow pattern past two spheres in proximity," *Phys. Fluids* **21**, 073603 (2009).
- ¹⁸D. H. Yoon and K. S. Yang, "Flow-induced forces on two nearby spheres," *Phys. Fluids* **19**, 098103 (2007).
- ¹⁹I. Kim, S. Elghobashi, and W. A. Sirignano, "Three-dimensional flow over two spheres placed side by side," *J. Fluid Mech.* **246**, 465–488 (1993).
- ²⁰L. Schouveiler, A. Brydon, T. Lewke, and M. C. Thompson, "Interactions of the wakes of two spheres placed side by side," *Eur. J. Mech. B/Fluids* **23**, 137–145 (2004).

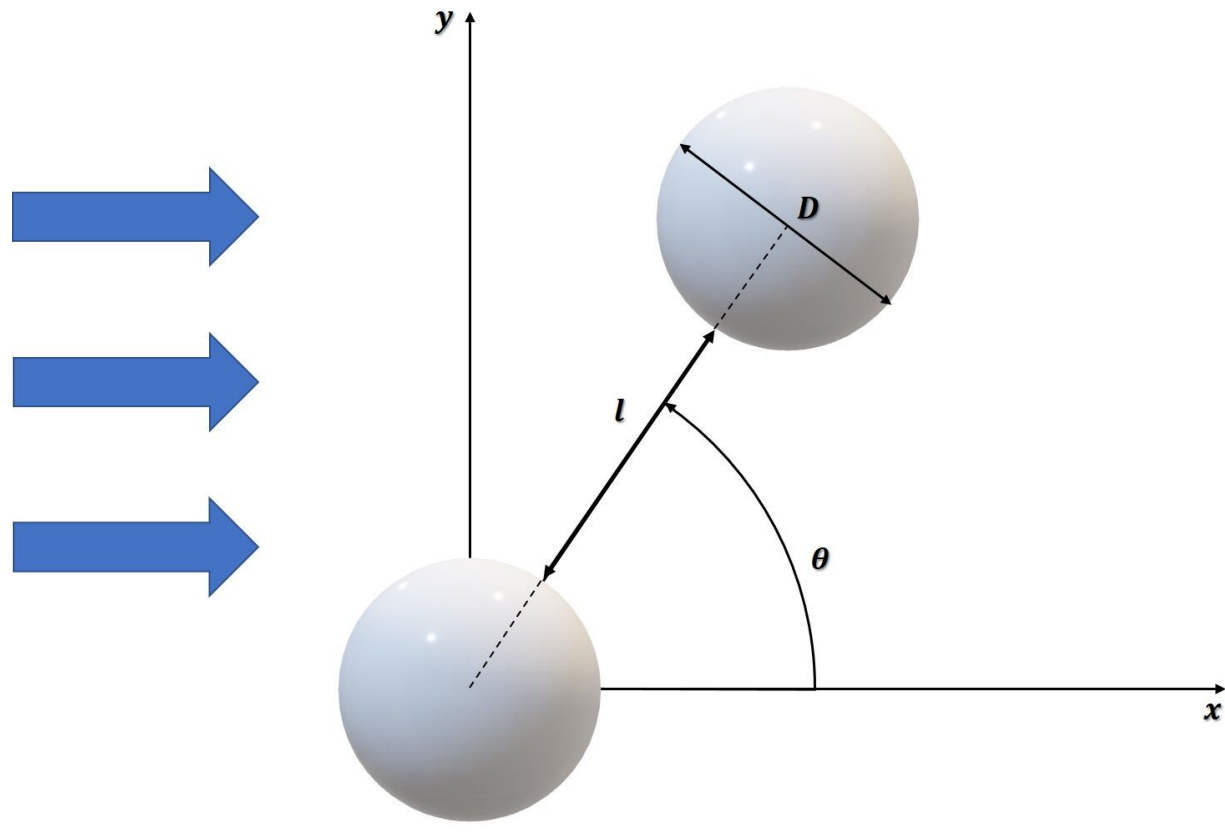
This is the author's peer reviewed, accepted manuscript. However, the online version of record will be different from this version once it has been copyedited and typeset.

PLEASE CITE THIS ARTICLE AS DOI: 10.1063/5.0044801

- ²¹C. Zhu, S. C. Liang, and L. S. Fan, "Particle wake effects on the drag force of an interactive particle," *Int. J. Multiph. Flow* **20**, 117–129 (1994).
- ²²R. C. Chen and Y. N. Lu, "The flow characteristics of an interactive particle at low Reynolds numbers," *Int. J. Multiph. Flow* **25**, 1645–1655 (1999).
- ²³D. Choi and H. Park, "Flow around in-line sphere array at moderate Reynolds number," *Phys. Fluids* **30**, 097104 (2018).
- ²⁴J. Szmelter and P. K. Smolarkiewicz, "An edge-based unstructured mesh framework for atmospheric flows," *Comput. Fluids* **46**, 455–460 (2011).
- ²⁵C. Kühnlein, W. Deconinck, R. Klein, S. Malardel, Z. Piotrowski, P. Smolarkiewicz, J. Szmelter, and N. Wedi, "FVM 1.0: a nonhydrostatic finite-volume dynamical core for the ifs," *Geosc. Model Dev.* **12**, 651–676 (2019).
- ²⁶F. B. Lipps and R. S. Hemler, "A scale analysis of deep moist convection and some related numerical calculations," *J. Atmos. Sci.* **39**, 2192–2210 (1982).
- ²⁷F. B. Lipps, "On the anelastic approximation for deep convection," *J. Atmos. Sci.* **47**, 1794–1798 (1990).
- ²⁸P. K. Smolarkiewicz and J. Szmelter, "A nonhydrostatic unstructured-mesh soundproof model for simulation of internal gravity waves," *Acta Geophys.* **59**, 1109–1134 (2011).
- ²⁹P. K. Smolarkiewicz, J. Szmelter, and F. Xiao, "Simulation of all-scale atmospheric dynamics on unstructured meshes," *J. Comput. Phys.* **322**, 267–287 (2016).
- ³⁰P. K. Smolarkiewicz and L. G. Margolin, "On forward-in-time differencing for fluids: extension to a curvilinear framework," *Mon. Weather Rev.* **121**, 1847–1859 (1993).
- ³¹P. K. Smolarkiewicz and J. Szmelter, "Multidimensional positive definite advection transport algorithm (MPDATA): an edge-based unstructured-data formulation," *Int. J. Numer. Methods Fluids* **47**, 1293–1299 (2005).
- ³²P. K. Smolarkiewicz and J. Szmelter, "MPDATA: an edge-based unstructured-grid formulation," *J. Comput. Phys.* **206**, 624–649 (2005).
- ³³J. Szmelter and P. K. Smolarkiewicz, "MPDATA error estimator for mesh adaptivity," *Int. J. Numer. Methods Fluids* **50**, 1269–1293 (2006).
- ³⁴G. Karypis and V. Kumar, "A fast and high quality multilevel scheme for partitioning irregular graphs," *SIAM J. Sci. Comput.* **20**, 359–392 (1998).
- ³⁵J. Jeong and F. Hussain, "On the identification of a vortex," *J. Fluid Mech.* **285**, 69–94 (1995).
- ³⁶J. F. Zou, A. L. Ren, and J. Deng, "Study on flow past two spheres in tandem arrangement using a local mesh refinement virtual boundary method," *Int. J. Numer. Methods Fluids* **49**, 465–488 (2005).

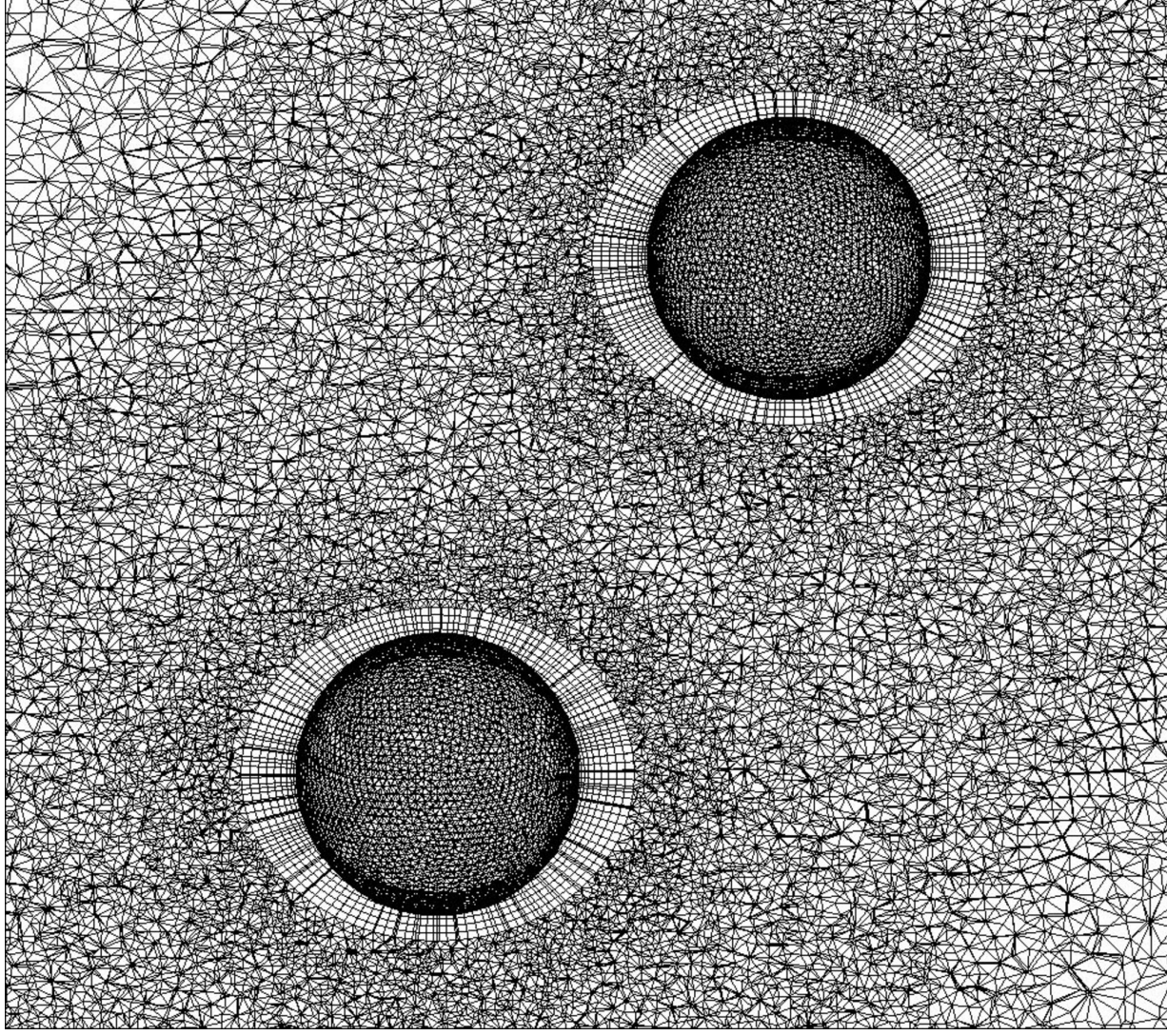
This is the author's peer reviewed, accepted manuscript. However, the online version of record will be different from this version once it has been copyedited and typeset.

PLEASE CITE THIS ARTICLE AS DOI: 10.1063/5.0044801



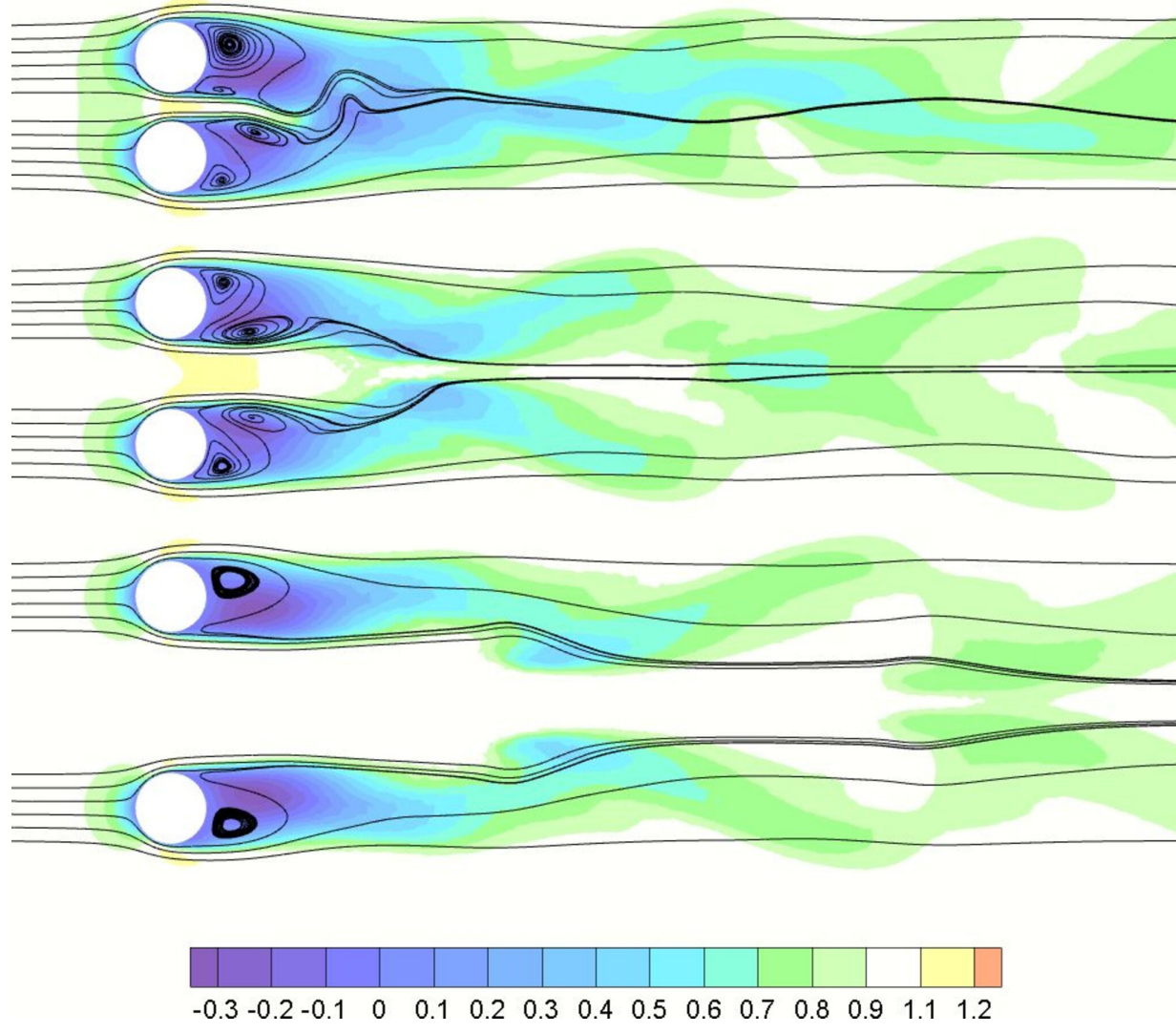
This is the author's peer reviewed, accepted manuscript. However, the online version of record will be different from this version once it has been copyedited and typeset.

PLEASE CITE THIS ARTICLE AS DOI: 10.1063/5.0044801



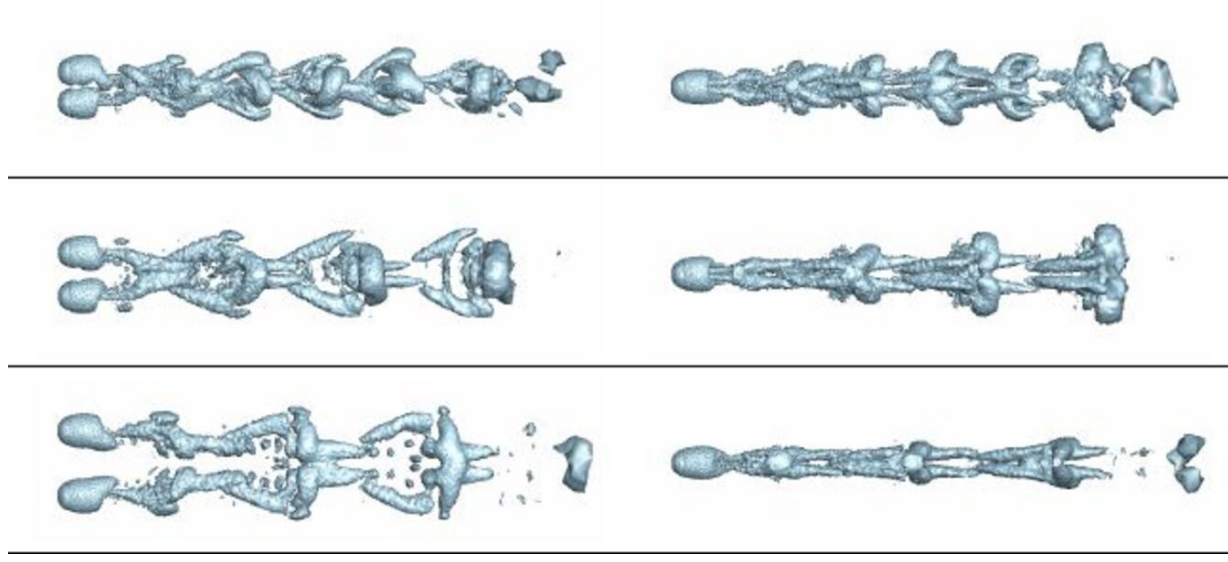
This is the author's peer reviewed, accepted manuscript. However, the online version of record will be different from this version once it has been copyedited and typeset.

PLEASE CITE THIS ARTICLE AS DOI: 10.1063/5.0044801



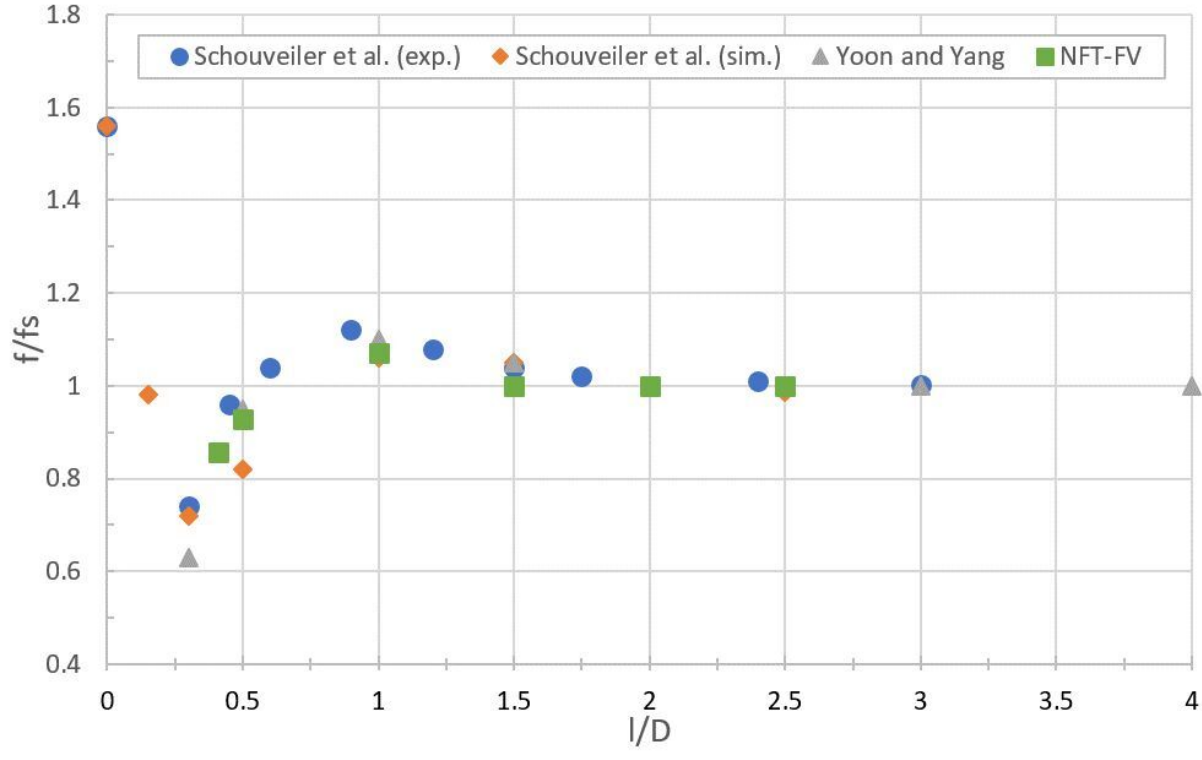
This is the author's peer reviewed, accepted manuscript. However, the online version of record will be different from this version once it has been copyedited and typeset.

PLEASE CITE THIS ARTICLE AS DOI: 10.1063/5.0044801



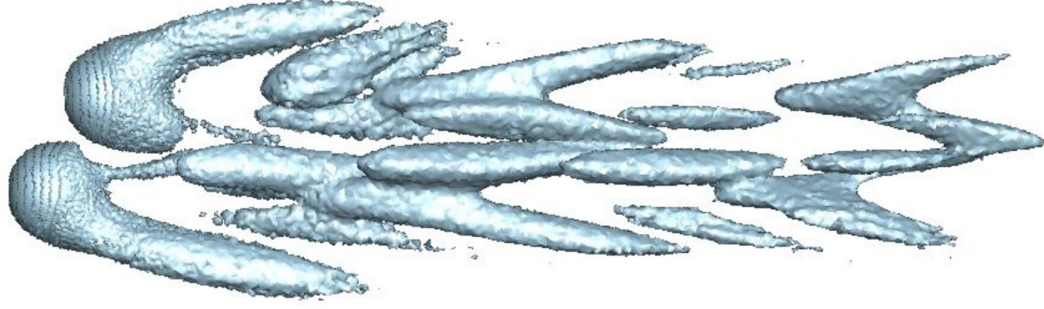
This is the author's peer reviewed, accepted manuscript. However, the online version of record will be different from this version once it has been copyedited and typeset.

PLEASE CITE THIS ARTICLE AS DOI: 10.1063/5.0044801



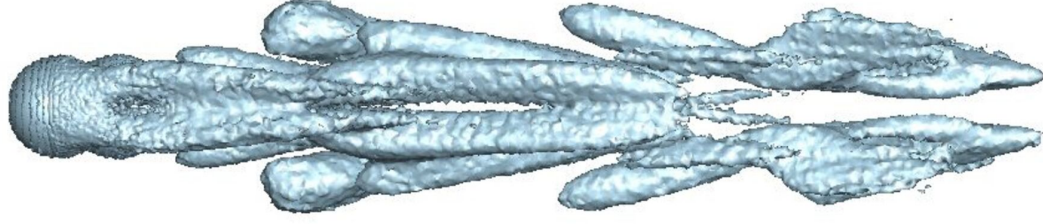
This is the author's peer reviewed, accepted manuscript. However, the online version of record will be different from this version once it has been copyedited and typeset.

PLEASE CITE THIS ARTICLE AS DOI: 10.1063/5.0044801



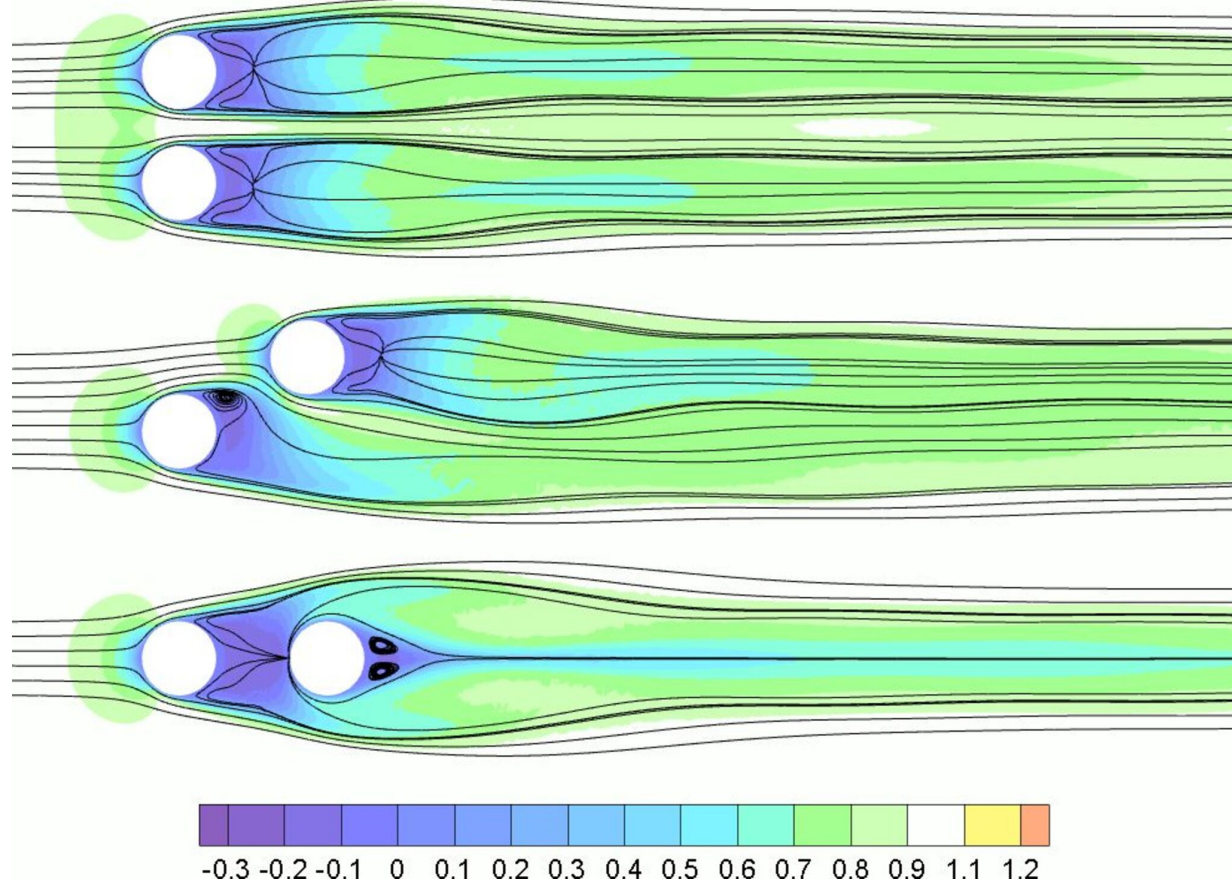
This is the author's peer reviewed, accepted manuscript. However, the online version of record will be different from this version once it has been copyedited and typeset.

PLEASE CITE THIS ARTICLE AS DOI: 10.1063/5.0044801



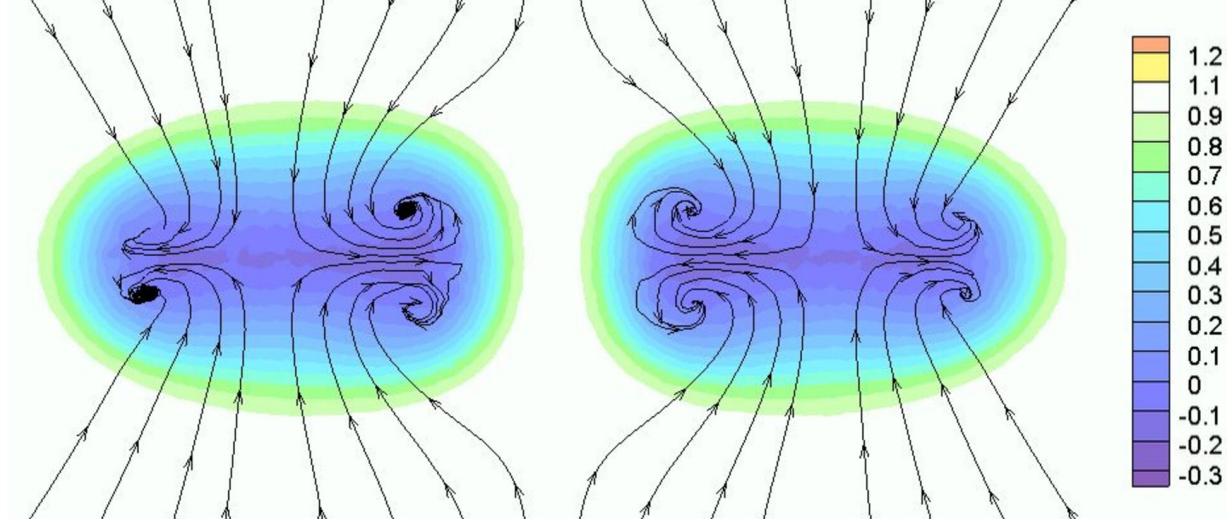
This is the author's peer reviewed, accepted manuscript. However, the online version of record will be different from this version once it has been copyedited and typeset.

PLEASE CITE THIS ARTICLE AS DOI: 10.1063/5.0044801



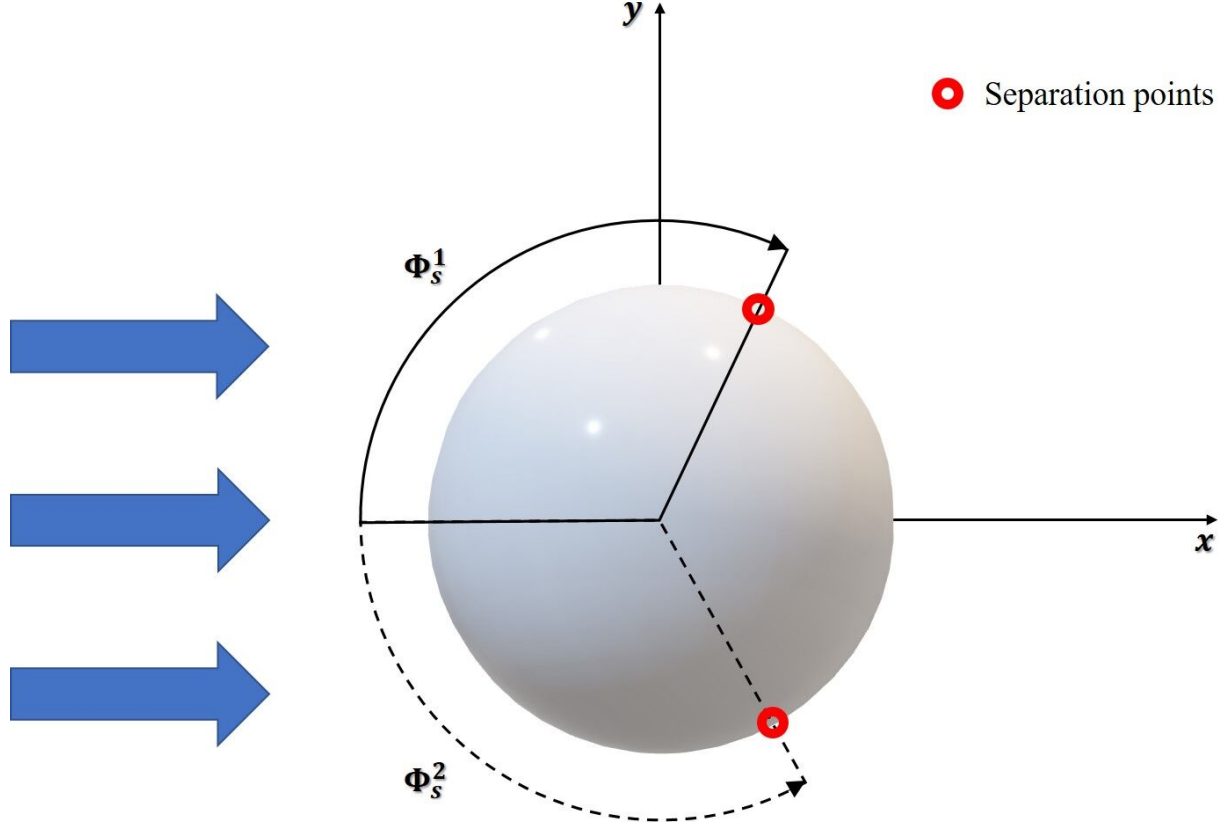
This is the author's peer reviewed, accepted manuscript. However, the online version of record will be different from this version once it has been copyedited and typeset.

PLEASE CITE THIS ARTICLE AS DOI: 10.1063/5.0044801



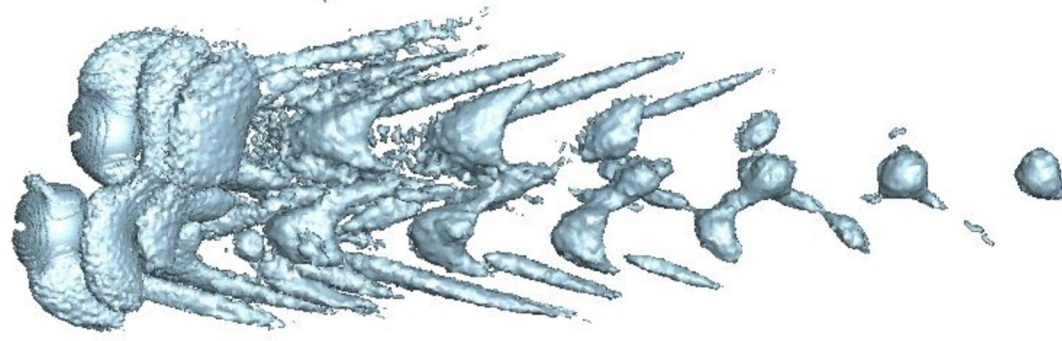
This is the author's peer reviewed, accepted manuscript. However, the online version of record will be different from this version once it has been copyedited and typeset.

PLEASE CITE THIS ARTICLE AS DOI: 10.1063/5.0044801



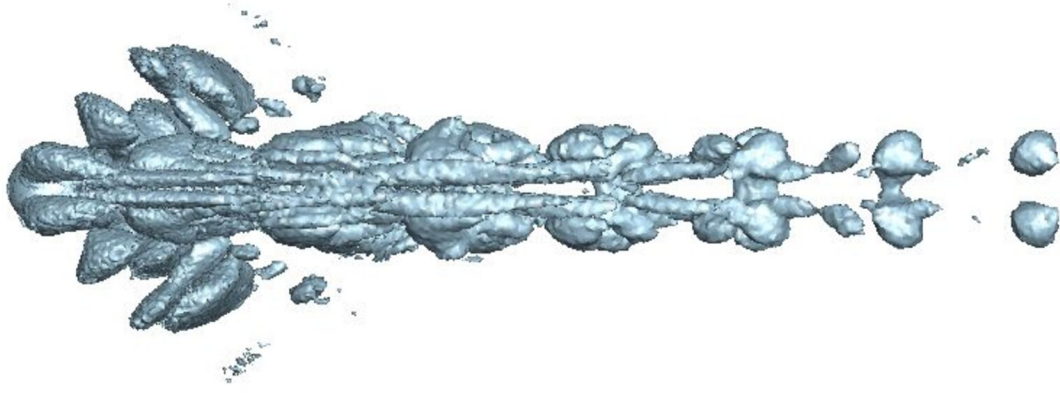
This is the author's peer reviewed, accepted manuscript. However, the online version of record will be different from this version once it has been copyedited and typeset.

PLEASE CITE THIS ARTICLE AS DOI: 10.1063/5.0044801



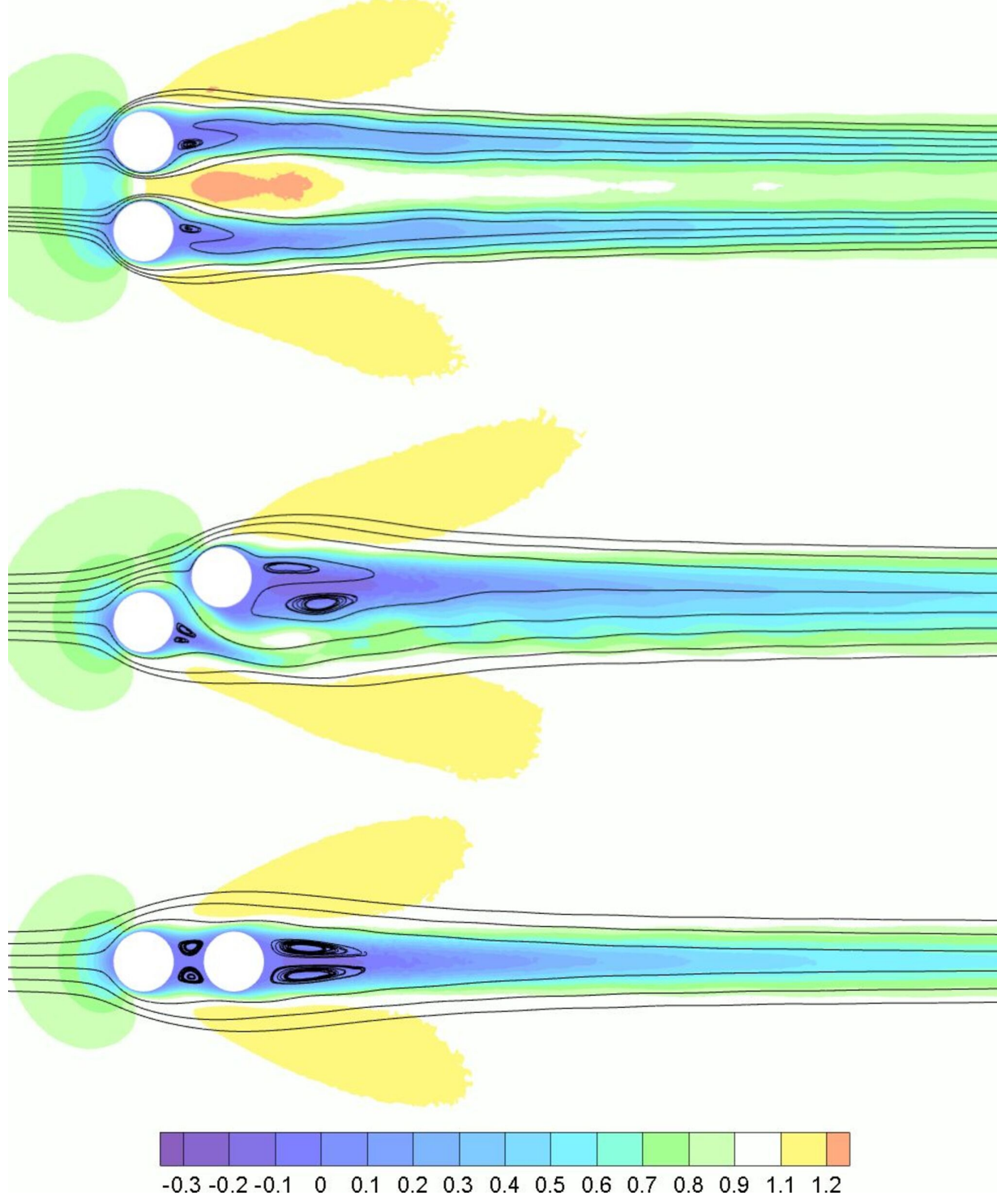
This is the author's peer reviewed, accepted manuscript. However, the online version of record will be different from this version once it has been copyedited and typeset.

PLEASE CITE THIS ARTICLE AS DOI: 10.1063/5.0044801



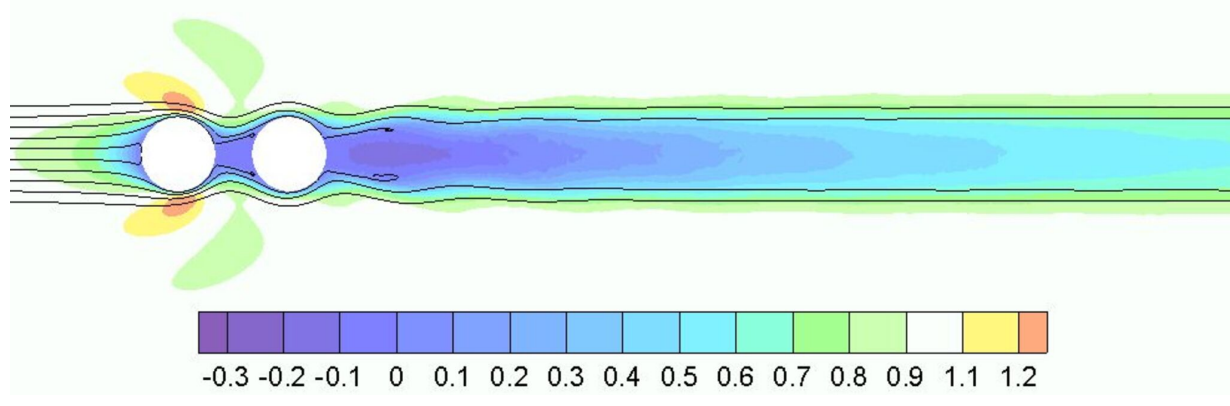
This is the author's peer reviewed, accepted manuscript. However, the online version of record will be different from this version once it has been copyedited and typeset.

PLEASE CITE THIS ARTICLE AS DOI: 10.1063/5.0044801



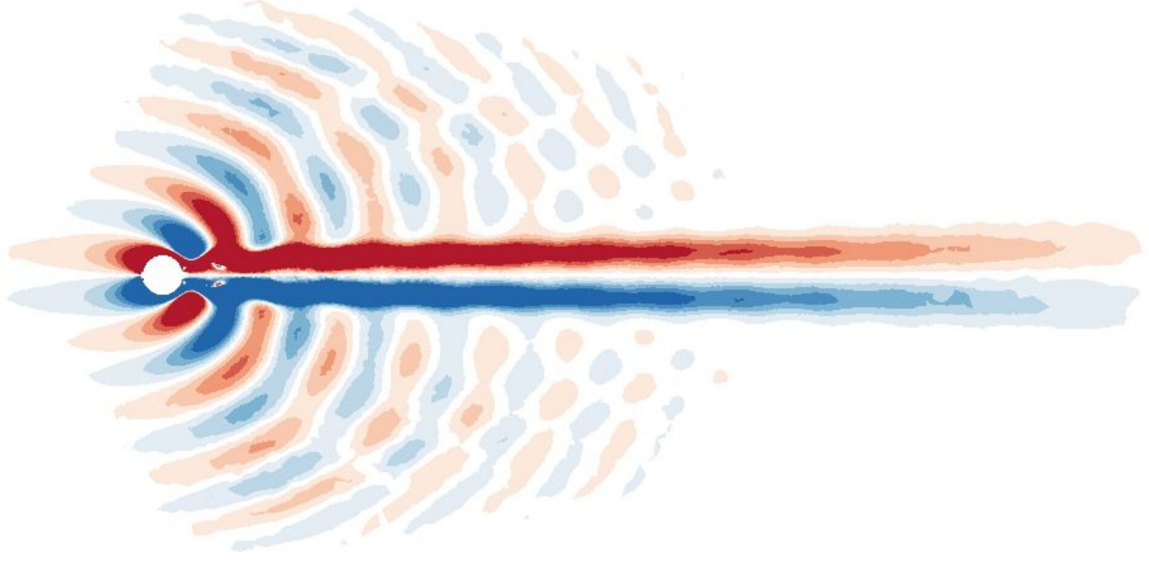
This is the author's peer reviewed, accepted manuscript. However, the online version of record will be different from this version once it has been copyedited and typeset.

PLEASE CITE THIS ARTICLE AS DOI: 10.1063/5.0044801



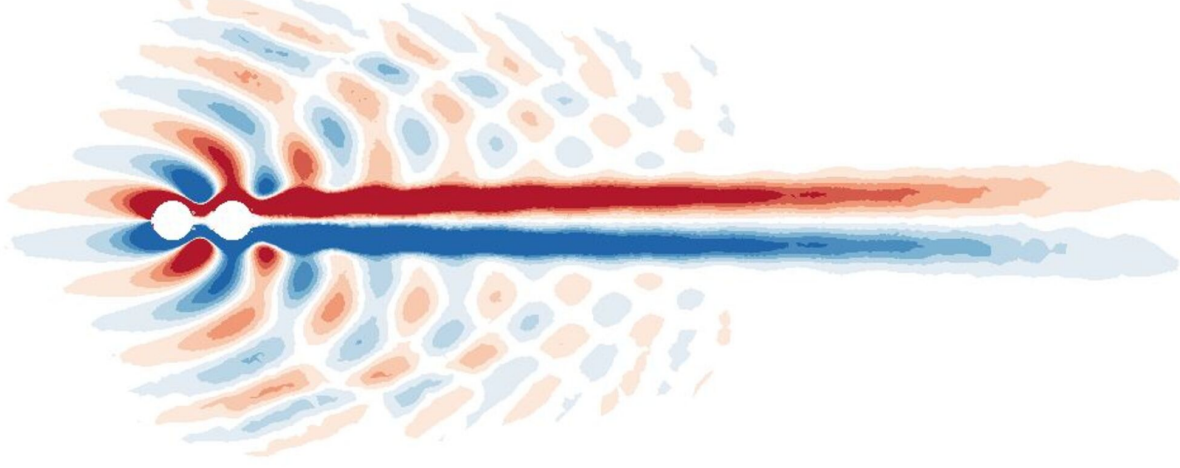
This is the author's peer reviewed, accepted manuscript. However, the online version of record will be different from this version once it has been copyedited and typeset.

PLEASE CITE THIS ARTICLE AS DOI: 10.1063/5.0044801



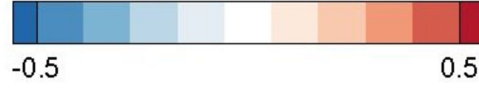
This is the author's peer reviewed, accepted manuscript. However, the online version of record will be different from this version once it has been copyedited and typeset.

PLEASE CITE THIS ARTICLE AS DOI: 10.1063/5.0044801



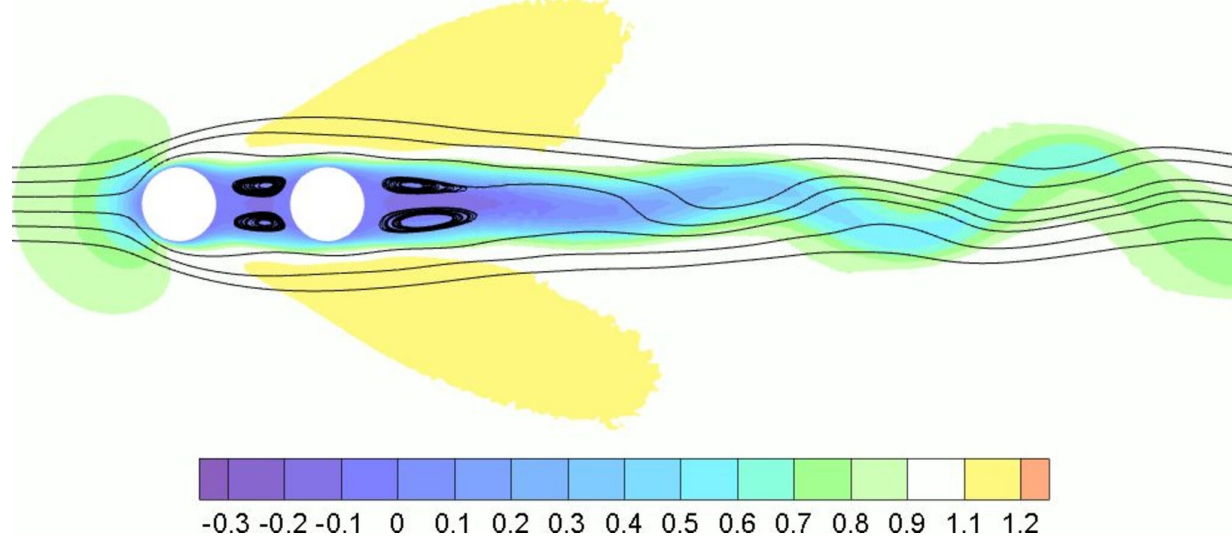
This is the author's peer reviewed, accepted manuscript. However, the online version of record will be different from this version once it has been copyedited and typeset.

PLEASE CITE THIS ARTICLE AS DOI: 10.1063/5.0044801



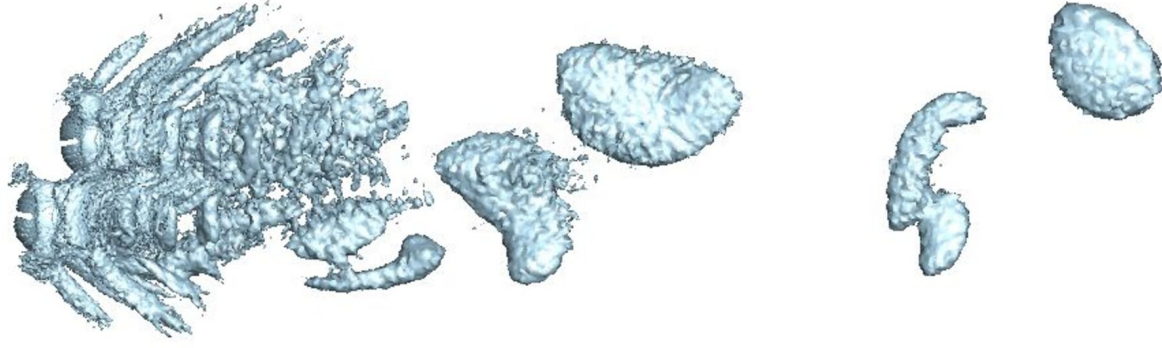
This is the author's peer reviewed, accepted manuscript. However, the online version of record will be different from this version once it has been copyedited and typeset.

PLEASE CITE THIS ARTICLE AS DOI: 10.1063/5.0044801



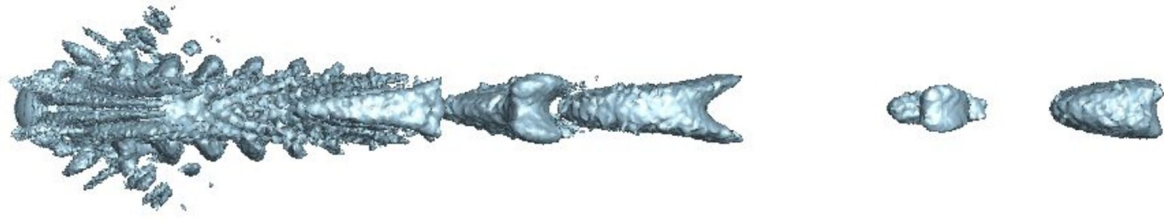
This is the author's peer reviewed, accepted manuscript. However, the online version of record will be different from this version once it has been copyedited and typeset.

PLEASE CITE THIS ARTICLE AS DOI: 10.1063/5.0044801



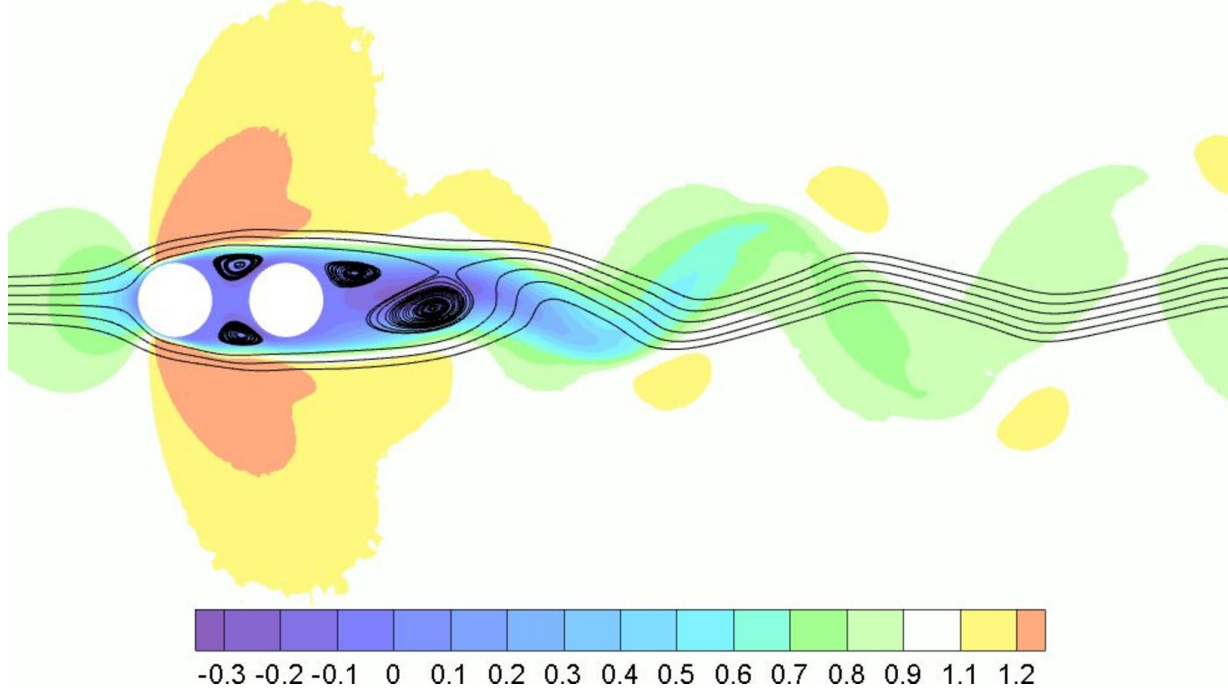
This is the author's peer reviewed, accepted manuscript. However, the online version of record will be different from this version once it has been copyedited and typeset.

PLEASE CITE THIS ARTICLE AS DOI: 10.1063/5.0044801



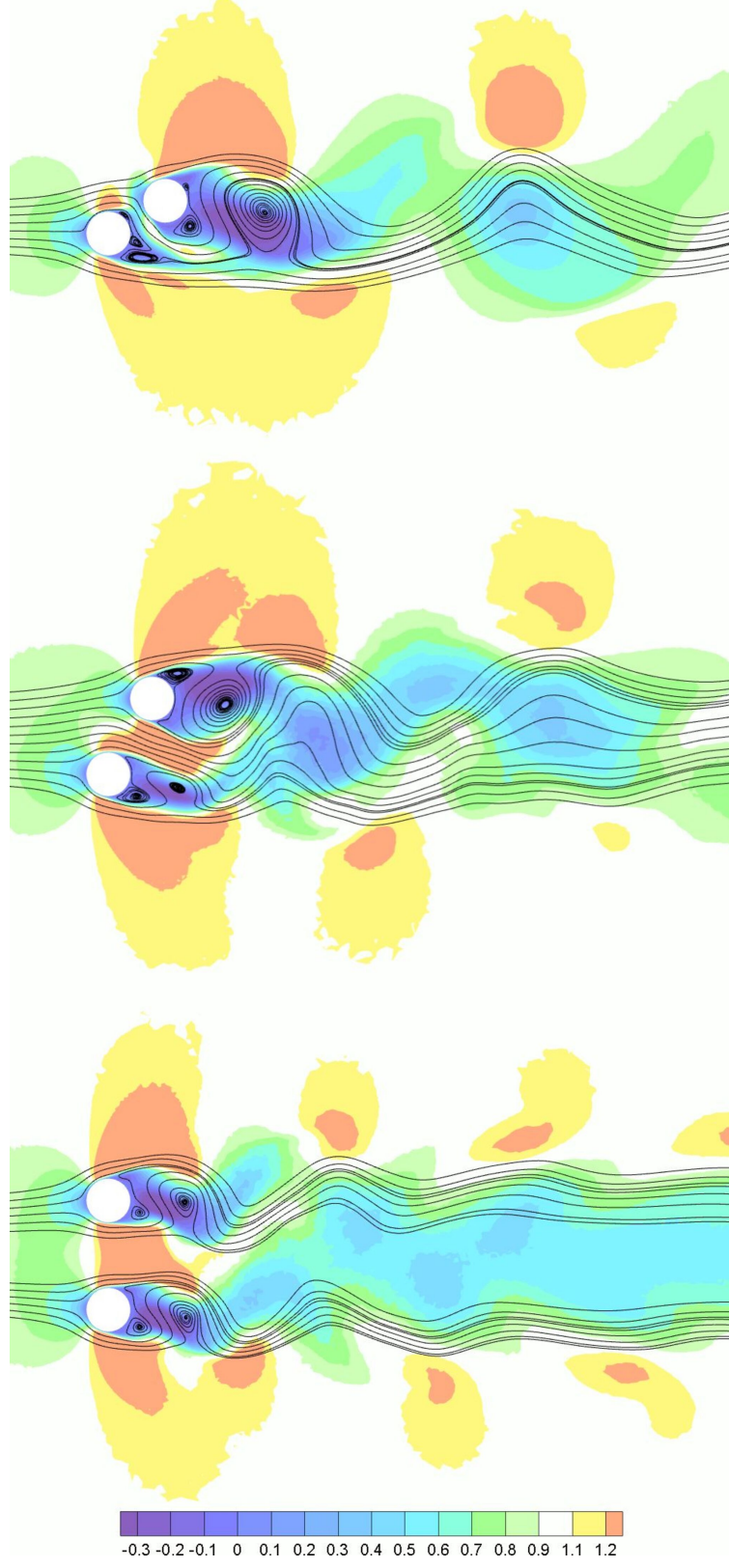
This is the author's peer reviewed, accepted manuscript. However, the online version of record will be different from this version once it has been copyedited and typeset.

PLEASE CITE THIS ARTICLE AS DOI: 10.1063/5.0044801



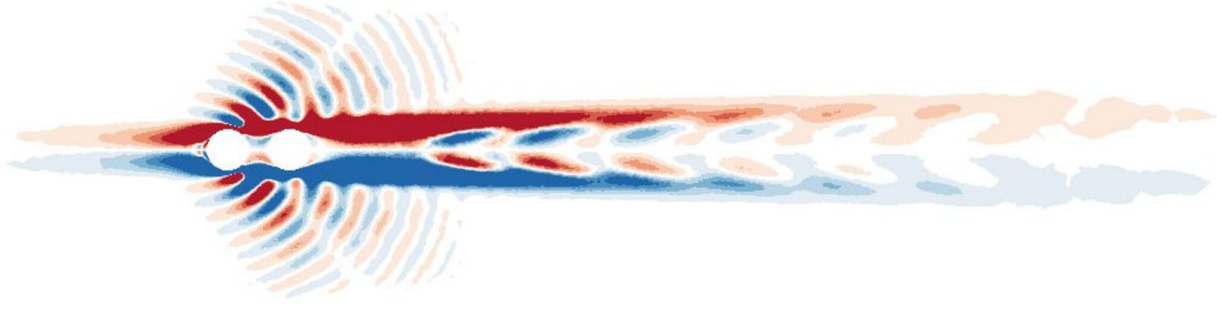
This is the author's peer reviewed, accepted manuscript. However, the online version of record will be different from this version once it has been copyedited and typeset.

PLEASE CITE THIS ARTICLE AS DOI: 10.1063/5.0044801



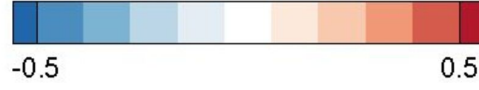
This is the author's peer reviewed, accepted manuscript. However, the online version of record will be different from this version once it has been copyedited and typeset.

PLEASE CITE THIS ARTICLE AS DOI: 10.1063/5.0044801



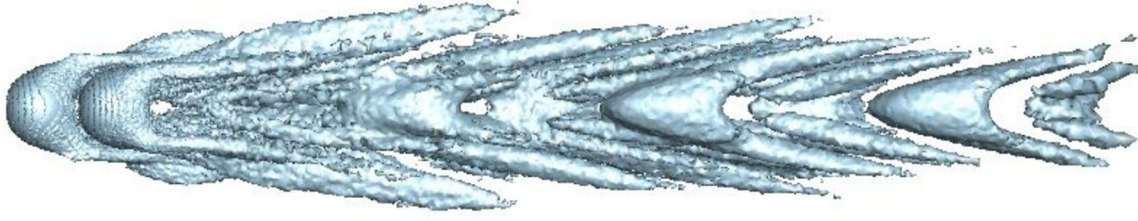
This is the author's peer reviewed, accepted manuscript. However, the online version of record will be different from this version once it has been copyedited and typeset.

PLEASE CITE THIS ARTICLE AS DOI: 10.1063/5.0044801



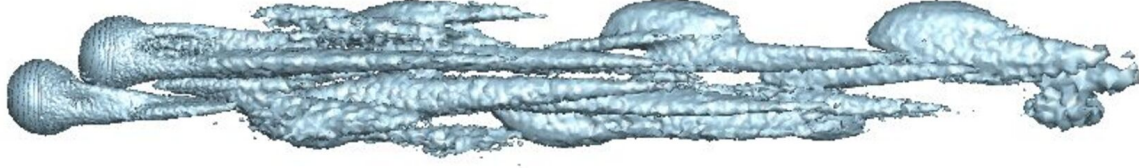
This is the author's peer reviewed, accepted manuscript. However, the online version of record will be different from this version once it has been copyedited and typeset.

PLEASE CITE THIS ARTICLE AS DOI: 10.1063/5.0044801



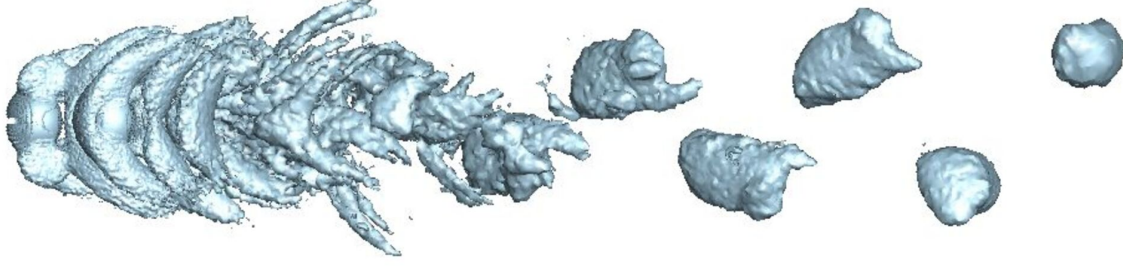
This is the author's peer reviewed, accepted manuscript. However, the online version of record will be different from this version once it has been copyedited and typeset.

PLEASE CITE THIS ARTICLE AS DOI: 10.1063/5.0044801



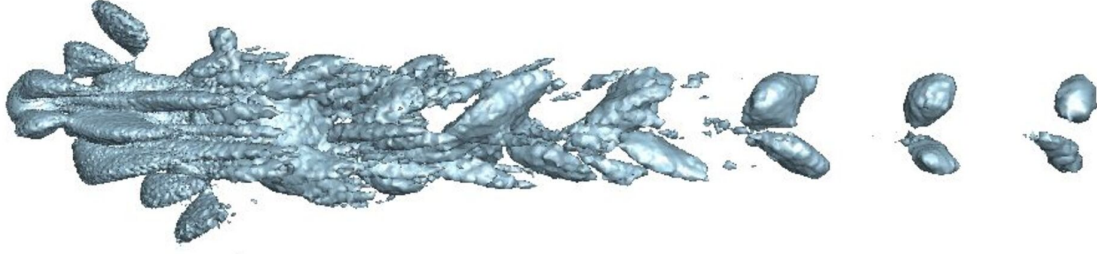
This is the author's peer reviewed, accepted manuscript. However, the online version of record will be different from this version once it has been copyedited and typeset.

PLEASE CITE THIS ARTICLE AS DOI: 10.1063/5.0044801



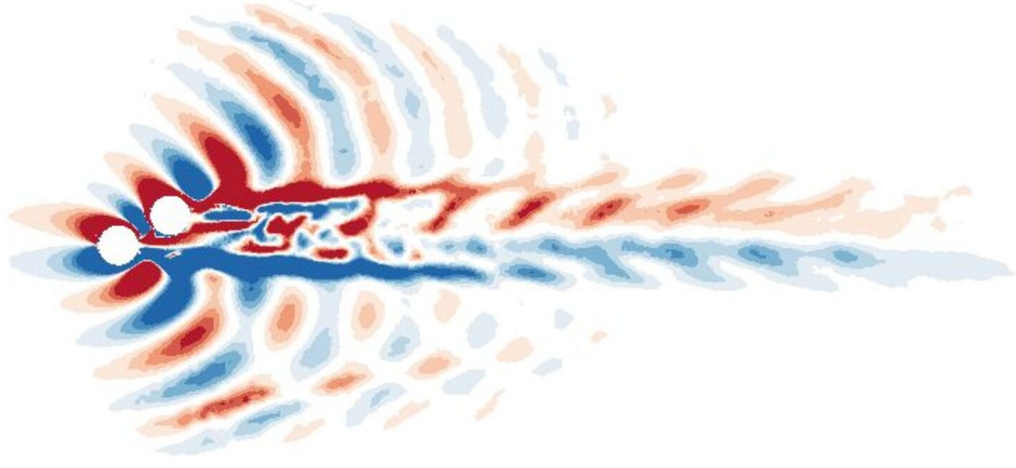
This is the author's peer reviewed, accepted manuscript. However, the online version of record will be different from this version once it has been copyedited and typeset.

PLEASE CITE THIS ARTICLE AS DOI: 10.1063/5.0044801



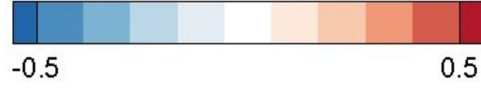
This is the author's peer reviewed, accepted manuscript. However, the online version of record will be different from this version once it has been copyedited and typeset.

PLEASE CITE THIS ARTICLE AS DOI: 10.1063/5.0044801



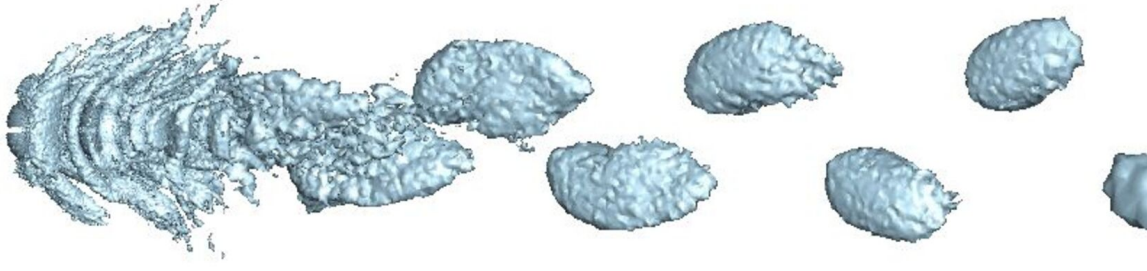
This is the author's peer reviewed, accepted manuscript. However, the online version of record will be different from this version once it has been copyedited and typeset.

PLEASE CITE THIS ARTICLE AS DOI: 10.1063/5.0044801



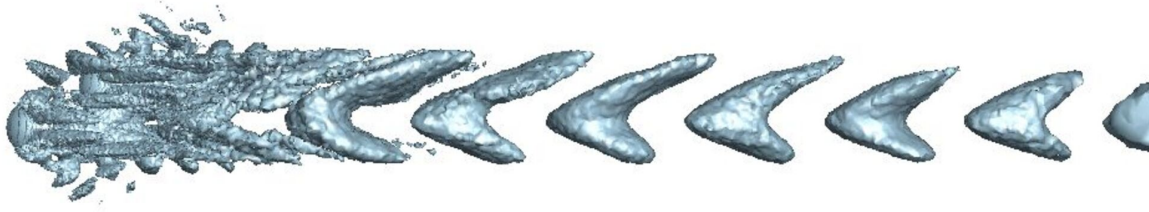
This is the author's peer reviewed, accepted manuscript. However, the online version of record will be different from this version once it has been copyedited and typeset.

PLEASE CITE THIS ARTICLE AS DOI: 10.1063/5.0044801



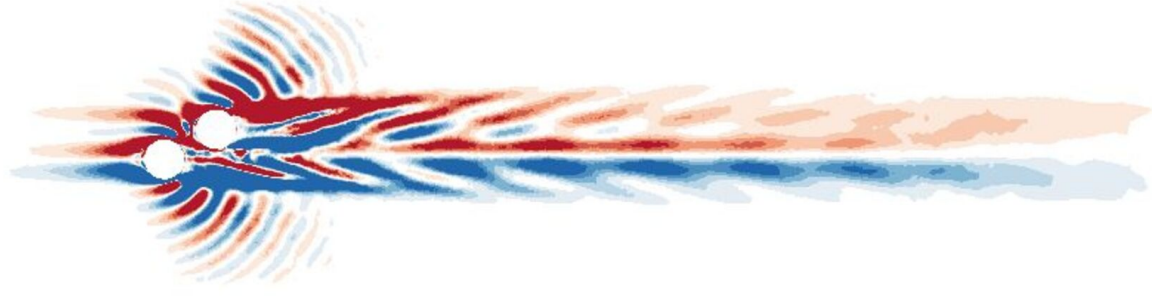
This is the author's peer reviewed, accepted manuscript. However, the online version of record will be different from this version once it has been copyedited and typeset.

PLEASE CITE THIS ARTICLE AS DOI: 10.1063/5.0044801



This is the author's peer reviewed, accepted manuscript. However, the online version of record will be different from this version once it has been copyedited and typeset.

PLEASE CITE THIS ARTICLE AS DOI: 10.1063/5.0044801



This is the author's peer reviewed, accepted manuscript. However, the online version of record will be different from this version once it has been copyedited and typeset.

PLEASE CITE THIS ARTICLE AS DOI: 10.1063/5.0044801

